Chemical propulsion of hemozoin crystal motion in malaria parasites

Erica M. Hastings[1,6], Tomasz Skora[2,6], Keith R. Carney[3], Henry C. Fu[4], Tamara C. Bidone[1,2,5], and Paul A. Sigala[1*]

[1]Department of Biochemistry, University of Utah School of Medicine, Salt Lake City, UT, United States
[2]Scientific Computing and Imaging Institute, University of Utah, Salt Lake City, UT, United States
[3]Huntsman Cancer Institute, University of Utah, Salt Lake City, UT, United States
[4]Department of Mechanical Engineering, University of Utah, Salt Lake City, UT, United States
[5]Department of Biomedical Engineering, University of Utah, Salt Lake City, UT, United States
[6]These authors contributed equally to this work

[*]Corresponding author: Paul Sigala
Email: p.sigala@biochem.utah.edu

Abstract

Malaria parasites infect red blood cells where they digest host hemoglobin and release free heme inside a lysosome-like organelle called the food vacuole. To detoxify excess heme, parasites form hemozoin crystals that rapidly tumble inside this compartment. Hemozoin formation is critical for parasite survival and antimalarial drug activity, but crystal motion and its underlying mechanism are unexplored. We used quantitative image analysis to determine the timescale of motion, which requires the intact vacuole but does not require the parasite itself. Using single-particle tracking and Brownian dynamics simulations with experimentally derived interaction potentials, we found that hemozoin motion exhibits unexpectedly tight confinement but is much faster than thermal diffusion. Hydrogen peroxide, which is generated at high concentrations in the food vacuole, has been shown to stimulate metallic nanoparticle motion via surface-catalyzed peroxide decomposition that generates propulsive kinetic energy. We observed that peroxide stimulated the motion of isolated crystals in solution and that conditions that suppress peroxide formation slowed hemozoin motion inside parasites. These data suggest that surface-exposed metals on hemozoin catalyze peroxide decomposition to drive crystal motion and strengthen oxidative stress protection during blood-stage infection. This work reveals hemozoin motion in malaria parasites as a biological example of a self-propelled nanoparticle.

Main text:

Malaria remains a deadly infectious disease that kills over 600,000 people each year and is caused by *Plasmodium* parasites that invade and destroy red blood cells (RBCs).[1] During blood-stage infection, parasites digest most of the RBC hemoglobin within an acidic food vacuole (FV) that is similar to a mammalian lysosome.[2] Hemoglobin proteolysis releases large quantities of the iron-containing cofactor, heme, which parasites detoxify by forming multiple ~500 nm brick-shaped hemozoin crystals within the ~1 µm-radius FV (**Fig. 1a**).[3,4] The biocrystallization of heme is a critical parasite survival strategy and major antimalarial drug target, such that free heme that escapes incorporation into crystals is thought to underpin chloroquine activity and serve as the key activator of frontline artemisinin therapies.[5,6]

Within the FV organelle, hemozoin crystals dynamically tumble in a rapid and unpredictable fashion (**Supplementary Video 1**).[7-10] Although ubiquitous, these dynamics are sparsely studied and have been described as Brownian in nature.[7,8] However, prior chemical and genetic perturbations of the FV have provided evidence that hemozoin motion can be stopped, suggesting additional energy inputs beyond thermal diffusion (**Supplementary Video 2, Extended Data Fig. 1a**).[9-11] Previous studies also provide conflicting evidence about whether hemozoin tumbling requires a physiologically active cell and thus serves as a biomarker of parasite viability or responds to local properties of the FV environment independent of the parasite.[7-10] Therefore, uncovering the physical nature and causative mechanism of crystal dynamics is key to unlocking a full understanding of hemozoin and its critical function in malaria parasite survival and drug susceptibility.

Hemozoin tumbling occurs on ms timescale. The rapid movement of hemozoin crystals is a hallmark of RBC infection by *P. falciparum*, which is the most virulent parasite species in Africa and causes nearly all human malaria deaths. To determine the timescale of hemozoin dynamics within the FV, we imaged *P. falciparum*-infected RBCs with brightfield microscopy using progressively faster frame rates (**Extended Data Fig. 1b**). We observed that the pixel intensity change between consecutive frames within the FV region decreased with increasing frame rate until plateauing at ~200 frames per second (Δt = 5 ms) (**Fig. 1b**). This observation indicates that the fastest detectable displacements of hemozoin crystals occur on a 5 ms timescale. Therefore, we used a frame rate of ≥200 frames per second for all subsequent imaging.

Hemozoin motion is a local FV property. To better understand the nature and origin of hemozoin motion within the FV, we sought to quantify the movement of individual crystals. Single-particle tracking (SPT) was unsuccessful due to crystal congestion and spatially overlapping trajectories in live parasites. To overcome this challenge, we developed an alternative method that quantified the mean squared pixel intensity change (TAMSI) within the FV as a function of elapsed time, which we define as "pixel velocity" (**Supplementary Video 3, Fig. 1c, Extended Data Fig. 2a-c**). This analysis revealed >10-fold differences between hemozoin motion in live versus dead (drug-inactivated) parasites, suggesting that the physiological condition of the FV underpins crystal dynamics (**Fig. 1d, Extended Data Fig. 2d, Extended Data 6**). To further probe the biological requirements for hemozoin motion, we fractionated parasites and tested various conditions for crystal motion. We measured hemozoin crystal TAMSI in fractionated intact parasites and isolated FVs and observed nearly identical pixel velocities across all conditions except dead parasites (**Fig. 1d, Extended Data Fig. 2a-d**). These findings indicate that hemozoin motion is a local property of the biochemically active FV environment and independent of the parasite's cellular context. However, this motion stops in lethally drug-treated parasites, suggesting a loss in FV membrane integrity and/or physiological activity in dead parasites.

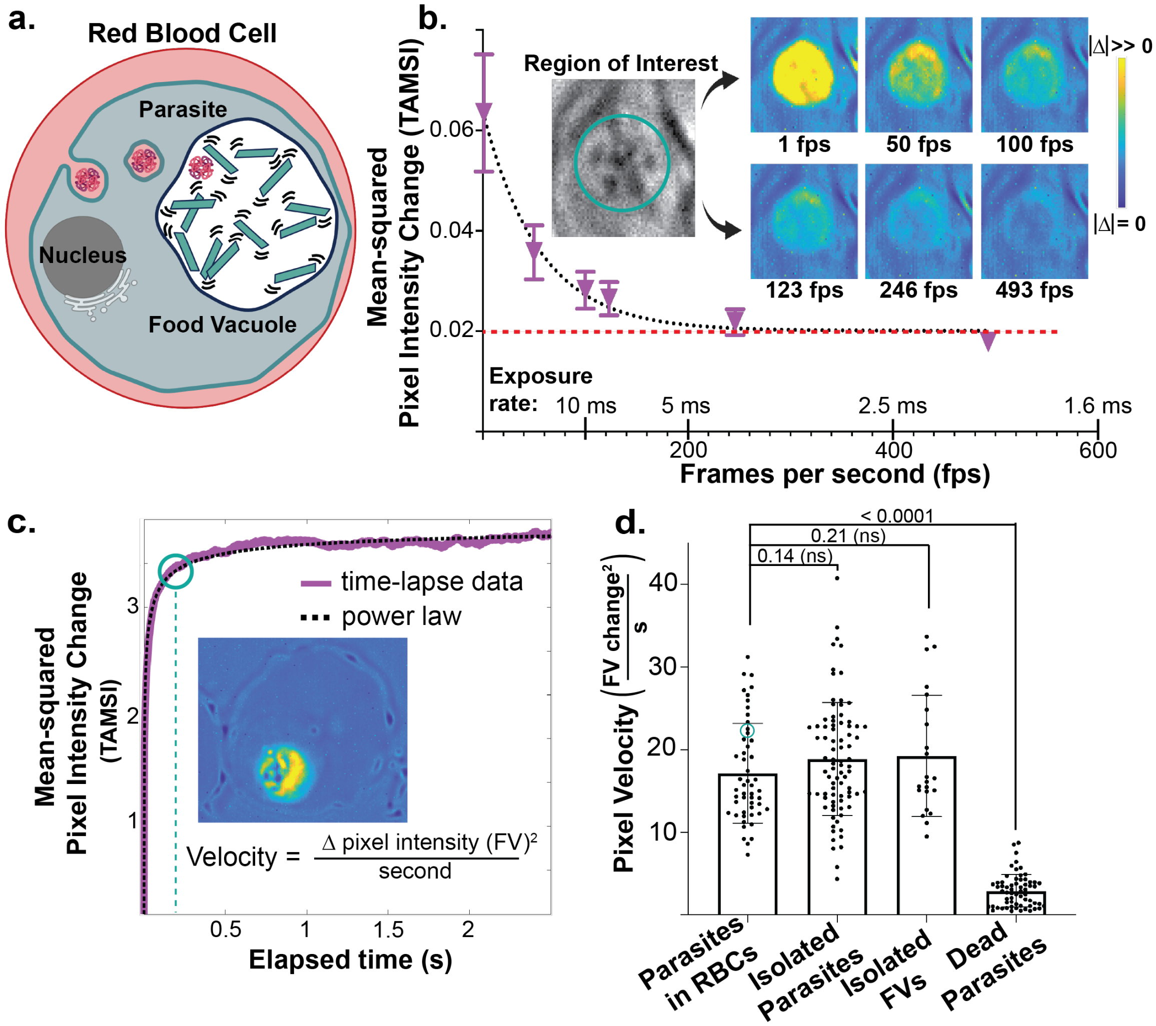

Figure 1: Quantification of hemozoin motion and its dependence on the FV environment. a, Diagram of a parasite-infected RBC, trafficking of host hemoglobin to the food vacuole, and formation of moving hemozoin crystals. **b**, Parasite FV regions of interest (inset) were imaged for variable exposure times. The pixel intensity change (Δ) in the region of interest was plotted versus time differences between frames. Heat map images (inset) show the gradient of pixel intensity

changes, with yellow pixels indicating largest change and dark blue pixels indicating smallest change. Pixel intensity change dependence on frame rate was empirically fit to an exponential decay equation (black dotted line). Red dashed line indicates lower limit of background camera detection. **c**, Plots of time-averaged mean squared pixel intensity change (TAMSI) within the FV region as a function of elapsed time revealed a plateau (decorrelation) beyond 0.2 s. Data were fit with a power-law growth function, provided in Methods, to determine the average time to plateau. An apparent pixel velocity was determined by dividing the TAMSI value at the average plateau time of 0.18 s in native parasites (teal circle). **d**, Population analysis of pixel velocities for FVs in live, fractionated, or dead (drug-treated) parasites. Teal circle shows pixel velocity of FV analyzed in Fig. 1c. Dead parasites were treated with a lethal dose of chloroquine (shown) or other antimalarial drugs. Hemozoin motion stopped in all treatments. Statistical analysis was done by Student's t-test to determine the indicated p-values. Error bars represent the standard deviation of the mean.

Single-particle tracking of crystal motion. To overcome FV congestion and enable accurate single-particle tracking (SPT) analysis of crystal displacements, we expanded the vacuoles using hypotonic conditions previously observed to enlarge mammalian lysosomes.[12-14] This expansion increased FV radii from ~1 μm to ~3 μm while preserving the rotational and translational components of hemozoin crystal motion (**Supplementary Video 4**, **Fig. 2a, Extended Data Fig. 3a**). Critically, the trajectories of individual crystals within expanded FVs could be reliably tracked for up to half a second (≥ 100 frames) to enable detailed analyses of their motion (**Fig. 2a**).

Within expanded FVs, we collected over 3500 trajectories of individual hemozoin crystals and analyzed their time-averaged mean squared displacements (TAMSDs) (**Extended Data Fig. 3c**). The weighted average of these TAMSDs as a function of elapsed time showed an anomalous nonlinear time dependence with a diminishing slope (**Fig. 2b-c,**). This observation contradicts predictions for simple diffusion based on the Einstein-Smoluchowski equation, where the TAMSD increases linearly with time ($MSD = 4Dt$).[15-18] Instead, the TAMSD data for hemozoin crystals in the FV were best fit by a power law ($MSD = 4\Gamma t^{\alpha}$), with an α value <1 indicative of subdiffusion (**Fig. 2c**).[19]

To compare the anomalous motion of FV hemozoin crystals to conditions where purely diffusive motion is expected, we isolated hemozoin crystals and suspended them in aqueous solutions of variable viscosity (**Fig. 2a**). Viscosity within the parasite FV is unknown but expected to be similar to a mammalian lysosome, ~ 100 – 400 cP.[20-23] Based on these values, we estimated the viscosity of expanded vacuoles due to water influx to be 10 – 40 cP, whose lower limit is equal to the viscosity of 60% w/v glycerol (aq) (**Extended Data Fig. 3b**). As expected, SPT of isolated hemozoin crystals or inert nanobeads in water or 60% glycerol displayed a linear time dependence

($\alpha \sim 1$), consistent with pure diffusion, while hemozoin motion within expanded FVs exhibited nonlinear behavior ($\alpha = 0.64 \pm 0.12$) (**Fig. 2b, Supplementary Table 1, Extended Data Fig. 3b**).

Based on fits to the power law form of the Einstein-Smoluchowski equation, hemozoin within expanded FVs had a generalized diffusion coefficient (Γ) of ~ 0.17 $\mu m^2/s^\alpha$, which was intermediate between that of isolated hemozoin in water (~ 1.1 $\mu m^2/s^\alpha$, 1 cP) and in 60% glycerol (~ 0.10 $\mu m^2/s^\alpha$, 10 cP). The enhanced (faster) diffusion of hemozoin in FVs compared to 60% glycerol was particularly prominent, given the expectation that both environments have similar viscosities. Possible explanations for this difference in slope include inaccuracy in FV viscosity, which may be less than 10 cP, or the presence of additional factors within the FV that stimulate crystal motion.

To test the accuracy of our estimated viscosity in expanded FVs, we analyzed the distribution of normalized crystal step sizes ($\mu m/s^{1/2}$) for hemozoin in expanded FVs, 60% glycerol (10 cP), or a thinner solution of 40% glycerol (4 cP). For a spherical particle of radius 0.2 µm, Brownian motion theory predicts a characteristic distribution of particle steps centered around ~ 0.6 $\mu m/s^{1/2}$ at a viscosity of 10 cP or ~1.2 $\mu m/s^{1/2}$ at 4 cP.[15-18] We observed a most frequent step size of ~ 0.6 $\mu m/s^{1/2}$ for hemozoin in expanded FVs and isolated crystals in 60% glycerol (**Fig. 2d, Extended Data Fig. 3d-e**). In contrast, isolated crystals in 40% glycerol displayed a recurring step size of ~1.2 $\mu m/s^{1/2}$ that was two-fold larger than FV hemozoin (**Extended Data Fig. 3d-e**). The close agreement between peak frequency of hemozoin step sizes within expanded FVs and 60% glycerol (10 cP) and disagreement with the larger average step sizes in 40% glycerol (4 cP) strongly support the conclusion that expanded FVs have an effective viscosity of 10 cP and that the motion of FV hemozoin is faster than predicted for thermal diffusion at this viscosity.

Further dissection of the histograms revealed that hemozoin in expanded FVs exhibited a heavier tail of longer step sizes compared to crystals in 60% glycerol (**Fig. 2d, inset**). To quantify this difference, we attempted to fit both distributions to a single population of moving particles. The 60% glycerol histogram was accurately fit by this model, which indicated a single population of particles with a diffusion coefficient of ~ 0.17 $\mu m^2/s$. However, the same fit to the histogram of crystals in expanded FVs could not be explained by a single population and instead revealed that the distribution was more accurately decomposed into two populations, with 33% of crystals having an expected diffusion coefficient (D_1) of 0.13 $\mu m^2/s$ and 67% of crystals with a much higher (faster) diffusion coefficient (D_2) of 0.63 $\mu m^2/s$ (**Extended Data Fig. 3e, Supplementary Table 5**). Since D_1 is close to the expected D for thermal diffusivity in 60% glycerol, we interpret the first population as purely diffusive particles. The second, faster-moving population for FV hemozoin suggests either that the size variation of hemozoin crystals differed between FVs and the glycerol environment or that an additional energy source transiently accelerates crystal diffusion within the FV. To analyze the potential for size heterogeneity, we solved for the expected particle size at the faster diffusion coefficient. This analysis indicated that most particles would have to be smaller than the diffraction limit of light (radius of ~ 0.03 μm) to account for faster diffusion and therefore unlikely to be seen or tracked through a brightfield microscope.[24] Based on these findings, we conclude that the *Plasmodium* food vacuole viscosity is indeed similar to a mammalian lysosome and that crystal motion deviates from our simplified experimental models of Brownian diffusion with additional features of both confined and stimulated motion.

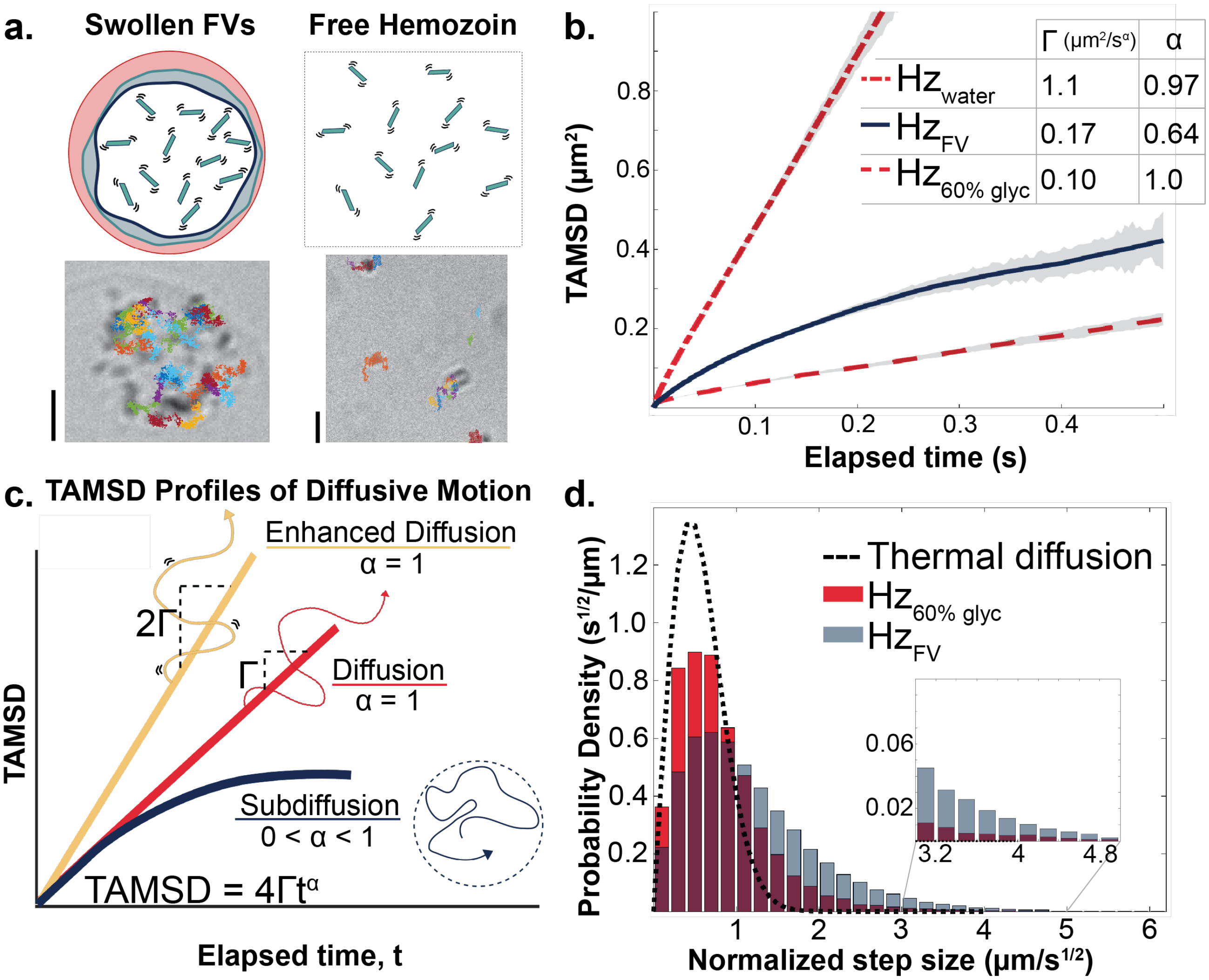

Figure 2: Expanded food vacuoles enable single-particle tracking and reveal enhanced but confined motion. a, Hypotonic conditions increase FV radius by ≥2-fold while maintaining crystal motion but avoiding crystal overlap (Supplementary Video 4). FV crystals are compared to isolated crystals in media with defined viscosities. Individual particle tracking showing longest tracks. Scale bars = 2 μm. **b**, Time-averaged mean squared displacement (TAMSD) of hemozoin crystals in expanded FVs compared to free hemozoin in matched viscosity and water with fit values

from Supplementary Table 1. Error bars represent the standard deviation of the means of individual trajectories and are shown in grey. **c**, Diffusion diagram showing generalized interpretations of TAMSD analysis. Γ is generalized diffusion coefficient ($\mu m^2/s^\alpha$), α is power law exponent. **d**, Histogram showing probability density of average step size (distance traveled) of each crystal over normalized time. Steps were normalized by dividing by square root time between beginning and end of step (due to varying elapsed times in data set). Maroon bins show overlapping data in probability distributions.

Simulated multi-particle crystal motion. Hemozoin crystals within the parasite FV have a cuboidal shape, are confined by the surrounding FV membrane, and interact with each other due to spatial crowding. These biophysical features differ from isolated crystals in solution or simple spheres modeled by the Einstein-Smoluchowski equation for simple Brownian motion. To determine if differences in crystal shape, FV boundary effects, and/or particle-particle interactions contribute to the faster but constrained diffusion of FV hemozoin, we performed stochastic Brownian dynamics simulations.[25] These simulations incorporated interaction potentials and boundary conditions designed to mimic expanded FV environments (**Extended Data Fig. 4a**). Specifically, we simulated diffusive motion of both hemozoin-shaped bricks and spherical particles under dimensional confinement conditions similar to those in our experiments and analyzed their trajectories to determine TAMSD values (**Supplementary Videos 5-6, Supplementary Table 6**). Cuboid bricks were modeled using surface-covering nodes with volume exclusion enforced by a repulsive Lennard-Jones potential (**Fig. 3a-b**). Simulations of spherical particles included both attractive and repulsive terms of the Lennard-Jones potential. This potential was parameterized from experimental SPT data of FV hemozoin using the Direct Boltzmann Inversion method and exhibited a very shallow minimum of -0.24 kcal/mol ($\ll k_B T$) at 0.82 μm, indicating weak attraction between crystals (**Fig. 3b, Extended Data Fig. 4b-c**).[26]

Simulated TAMSDs were adjusted to account for the static localization error in the experimental trajectories resulting from microscope noise that systematically offsets the observed particle position from the true position.[27] After making this correction, we observed a strong concordance between the simulated models and experimental SPT analysis of isolated hemozoin in water and 60% glycerol over 0.5 s (**Fig. 3c**). Using the power-law form of the Einstein-Smoluchowski equation to fit the simulated data, we determined α exponents of ≥ 0.85 and ≥ 0.98

for crystal motion at viscosities equal to water and 60% glycerol, respectively, despite particle-particle interactions and confinement within a spherical boundary of ~2.5 μm radius (**Supplementary Tables 6, 7, 8**). These results closely matched the experimental data for isolated hemozoin in these environments. Simulated TAMSDs in water showed a slight curvature toward subdiffusive behavior, consistent with the expectation that particles reach the simulated boundary sooner in this lower-viscosity environment. Most importantly, the α exponents in simulations were still significantly greater than the α exponent obtained experimentally for FV hemozoin (0.64 ± 0.12) (**Fig. 3c**; **Extended Data Fig. 4c; Supplementary Tables 6, 7, 8**). These findings suggest that differences in hemozoin shape, FV boundary constraints, and interactions between hemozoin crystals do not explain the faster and nonlinear time dependence of FV hemozoin motion.

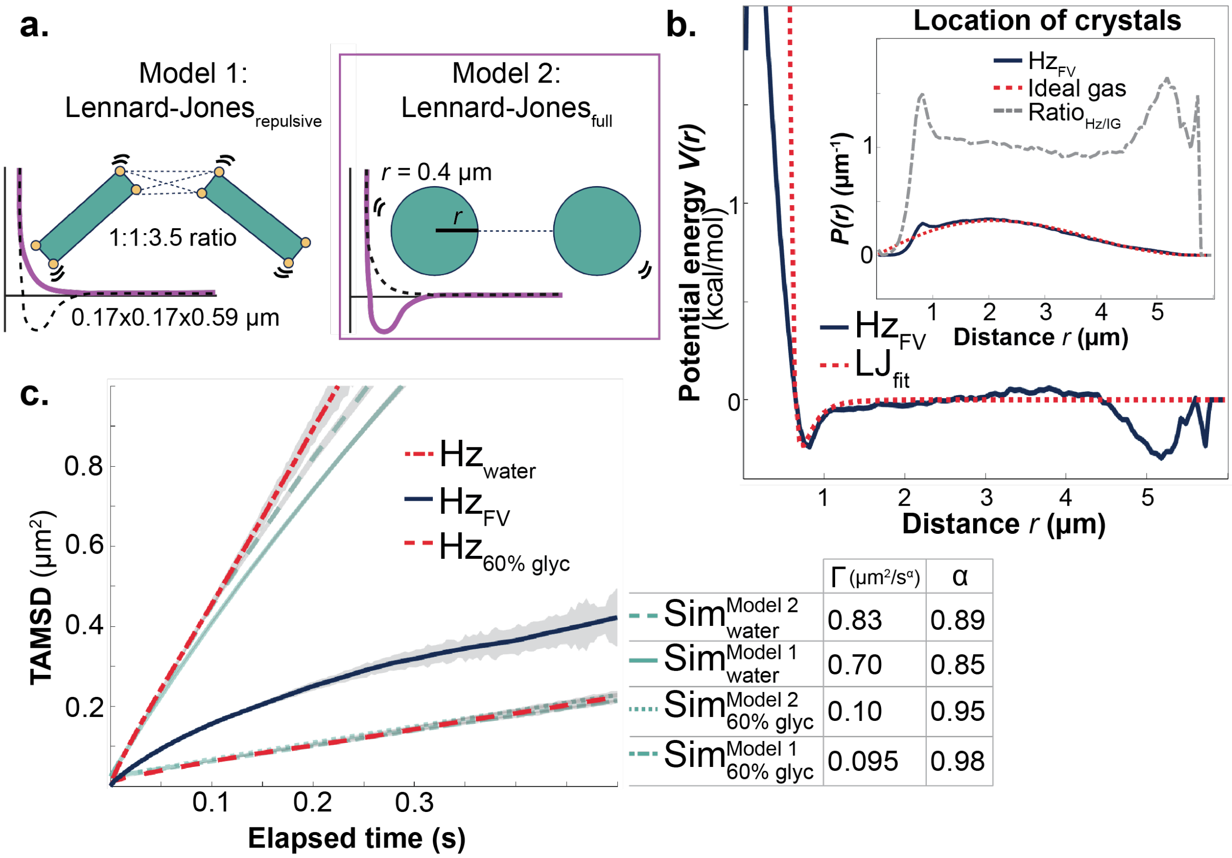

	Γ (μm²/s$^{\alpha}$)	α
Sim$^{Model 2}_{water}$	0.83	0.89
Sim$^{Model 1}_{water}$	0.70	0.85
Sim$^{Model 2}_{60\% glyc}$	0.10	0.95
Sim$^{Model 1}_{60\% glyc}$	0.095	0.98

Figure 3: Stochastic Brownian dynamics simulations of hemozoin crystal motion in distinct environments cannot account for anomalous FV features. a, Different geometric shapes and particle-particle interactions were used to compare Brownian models. Model 1 used cuboidal bricks with a repulsive Lennard-Jones interaction within a contact distance of 500 nm. Cuboidal shapes used dimensions as shown following previous literature.[4,28] Model 2 used simplified spheres of equal crystal volume with a full Lennard-Jones potential including attraction and repulsion. **b**, Experimental tracks were used to calculate the interaction potentials between crystals. The calculated interaction potential looked like a fully defined Lennard-Jones potential with weak attraction and then repulsion at the minimal distance between two crystals. Model 2 used these interaction potentials. Inset shows probability of crystal-crystal distance in experiment vs. in an ideal gas scenario. **c**, TAMSD of hemozoin crystals in expanded FVs compared to simulations from Models 1 and 2 from Fig. 3a. See Supplementary Tables 6, 7, 8 for fitted TAMSD values. Error bars represent the standard deviation of the means of individual trajectories and are shown in grey.

Propulsion and micro-confinements explain hemozoin motion. To understand the enhanced diffusivity and constrained TAMSD properties of FV hemozoin compared to isolated crystals, we further analyzed their TAMSD and normalized step-size distribution (**Fig. 2b,d**). The nonlinear shape of the hemozoin TAMSD in FVs aligns with theoretical predictions for particle diffusion where the TAMSD plateaus at ~ $0.8R^2$ within a sphere of radius R projected onto a 2D plane (**Fig. 4a**).[29] This prediction matches simulations of hemozoin in a FV-like environment but does not account for hemozoin motion in expanded FVs where the TAMSD levels off at values that are much smaller than expected (**Fig. 3c**). This discrepancy suggests that physical micro-confinements within the FV limit crystal motion to sub-compartments of ~ 1.1 µm radius that are 2-fold smaller than the expanded FV radius (~ 2.5 µm) (**Supplementary Table 6**). These additional barriers may be due to membranous remnants of vesicles that deliver host hemoglobin to the FV or other heterogeneities in the FV matrix that confine crystals.[30]

The enhanced diffusivity and heavy tails of longer step sizes of FV hemozoin suggested the possibility of energy inputs beyond thermal energy driving crystal motion (**Fig. 2d**). We first ruled out that white light of variable brightness affected hemozoin motion, as changing microscope light intensity from 1.8 to 25.3 mW/cm^2 did not alter the anomalous exponent or diffusion coefficients in expanded vacuoles (**Extended Data Fig. 5a**). We next tested a potential chemical origin for the enhanced diffusivity of FV hemozoin. Hydrogen peroxide (H_2O_2) is produced within the aerobic FV of parasites as a byproduct of hemoglobin digestion. This catabolic process releases ferrous heme, which oxidizes to form hemozoin and generates hydrogen peroxide from ambient O_2.[31,32] Malaria parasites do not encode catalase to degrade FV hydrogen peroxide, and how they neutralize this oxidative and cytotoxic stress remains unclear. Iron and other metals have been shown to catalyze hydrogen peroxide decomposition to release kinetic energy.[33-37] We hypothesized that catalysis of this reaction within the FV by surface-exposed metals on hemozoin stimulates crystal motion.

We tested this hypothesis by first asking whether 15% H_2O_2 enhanced the diffusivity of isolated hemozoin crystals in water. Using SPT, we observed a nearly 2-fold increase in the diffusion coefficient, which is comparable to previously reported motion enhancements for metallic nanoparticles based on this reaction (**Fig. 4b, Extended Data Fig. 5b, Supplementary Table 1**).[38,39] This "boost" was not observed for inert nanobeads in water (**Fig. 4b, Extended Data Fig. 5b, Supplementary Table 3**). Power-law analysis of hemozoin motion showed that 15% H_2O_2 did not substantially alter the α exponent from its value in water (α ~ 1) indicating enhanced diffusion (**Fig. 2c, Supplementary Table 1**). However, the step-size histogram for isolated hemozoin crystals in 15% H_2O_2 displayed a heavy tail of longer step sizes, surprisingly similar to the histogram of FV hemozoin but in contrast to isolated hemozoin in 60% glycerol (**Fig. 2d, Fig. 4c**). The experimental step-size histogram for isolated hemozoin in water (1 cP) was accurately fit to a single population with a diffusion coefficient of 1.44 $\mu m^2/s$ at a particle radius of 0.15 µm. In 15% H_2O_2, the histogram of crystal step sizes could only be accurately fit with a bimodal model where 38% of the crystal population had $D_1 \sim 0.9\ \mu m^2/s$ and the other 62% of crystal step sizes fit a $D_2 \sim 5.8\ \mu m^2/s$ (**Extended Data Fig. 5c**). The close similarity between D_1 and the thermal diffusion coefficient expected for 0.2 µm radius particles (1.1 $\mu m^2/s$) suggests a smaller population of purely diffusive crystals and a larger population of crystals whose ≥5-fold larger D_2 value resembles the enhancement ratio observed for FV hemozoin (**Supplementary Table 5, Extended Data Fig. 5c**).

We next investigated whether the crystal population with enhanced diffusivity could be explained by a simple model of random propulsion due to hemozoin surface catalysis of H_2O_2

decomposition. As a minimal model, we simulated 0.2 μm radius spherical particles undergoing thermal diffusion (D ~ 1.1 $\mu m^2/s$ in water) and subject to randomized propulsive velocities normally distributed around zero. For translational propulsive velocity, we found that choosing a standard deviation of 60 μm/s for each direction (x, y, z) produced a step-size distribution that matched the faster fraction in the bimodal fit. Combining the step-size distribution of this active population (62%) with that of a thermally diffusing population (D_1 ~ 0.9 $\mu m^2/s$, 38%) produced a step-size distribution like that observed experimentally (**Fig. 4c, Extended Data Fig. 5d**). Thus, our model for active propulsion of hemozoin by random catalysis of peroxide decomposition is sufficient to explain the experimental bimodal step-size distribution.

We next tested whether simulated particles in the estimated FV viscosity, with a smaller radial boundary of 1.1 μm and a bimodal distribution of step sizes parametrized from our hemozoin results in 15% H_2O_2, could quantitatively account for the enhanced diffusion and anomalous constraints of FV hemozoin. Inclusion of either the 1.1 μm radial boundary or the bimodal step-size distribution in simulations failed to match experiments, but including both properties nearly quantitatively matched the experimental TAMSD (**Fig. 4d**). The strong agreement between simulations and experiments supports our hypothesis that sub-compartmental constraints and chemical stimulation quantitatively explain the enhanced and anomalous features of FV crystal motion.

Hydrogen peroxide generation in the parasite FV is expected to depend on O_2 availability.[40] Our model predicts that a reduction in H_2O_2 concentration will suppress crystal motion. To test this prediction, we determined pixel velocities (TAMSI) for hemozoin moving within parasites grown and maintained at ambient 20% O_2 or at reduced O_2 tension of 2-3% (**Extended Data Fig. 5e**). Critically, parasites have a low respiratory requirement for O_2 and grow similarly in these two conditions.[41] In contrast to unchanged parasite growth, there was a ~2-fold reduction in pixel velocity for hemozoin motion in live parasites in 2% O_2 that remained faster than observed for dead parasites (**Fig. 4e**). This decrease in speed directly supports our model that H_2O_2 serves as a fuel for propelling crystal motion in the FV and that lowering peroxide concentration slows hemozoin dynamics.

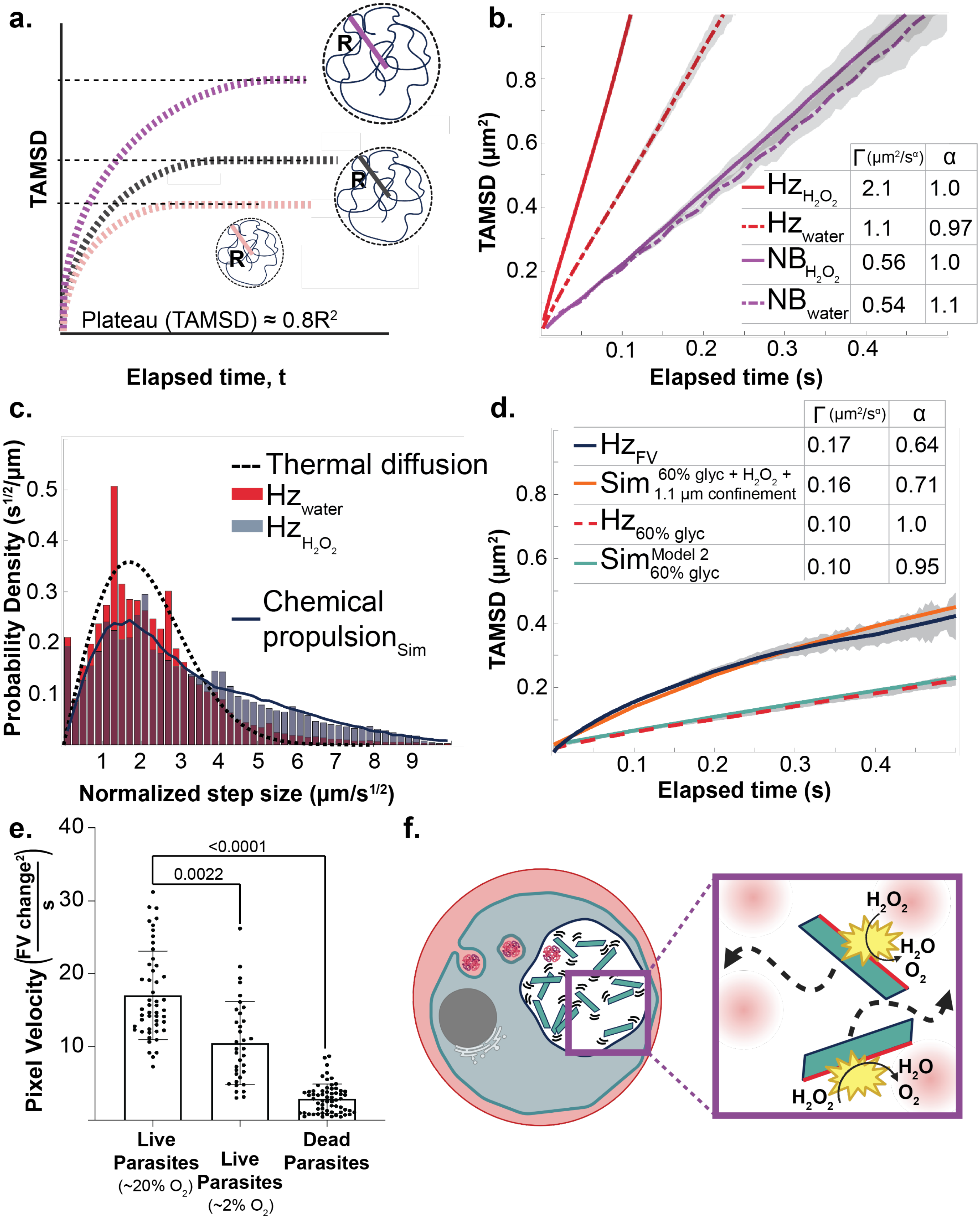
a.
TAMSD
R
R
R
Plateau (TAMSD) ≈ 0.8R²
Elapsed time, t
b.
TAMSD (μm²)
0.2
0.4
0.6
0.8
0.1
0.2
0.3
0.4
Elapsed time (s)
Γ (μm²/s^α) | α
Hz H2O2 | 2.1 | 1.0
Hz water | 1.1 | 0.97
NB H2O2 | 0.56 | 1.0
NB water | 0.54 | 1.1
c.
Probability Density (s^1/2/μm)
0.1
0.2
0.3
0.4
0.5
1 2 3 4 5 6 7 8 9
Normalized step size (μm/s^1/2)
--- Thermal diffusion
Hz water
Hz H2O2
Chemical propulsion Sim
d.
TAMSD (μm²)
0.2
0.4
0.6
0.8
0.1
0.2
0.3
0.4
Elapsed time (s)
Γ (μm²/s^α) | α
Hz FV | 0.17 | 0.64
Sim 60% glyc + H2O2 + 1.1 μm confinement | 0.16 | 0.71
Hz 60% glyc | 0.10 | 1.0
Sim Model 2 60% glyc | 0.10 | 0.95
e.
Pixel Velocity (FV change² / s)
10
20
30
40
<0.0001
0.0022
Live Parasites (~20% O2)
Live Parasites (~2% O2)
Dead Parasites
f.
H2O2
H2O
O2
H2O
O2
H2O2

Figure 4: Extra energy and smaller confinement are required to capture crystal trajectories in the FV. a, Diagram showing predicted TAMSD plots for variable confinement radii. **b**, TAMSD of hemozoin crystals and inert nanobeads in water versus 15% aqueous H_2O_2. Error bars represent the standard deviation of the means of individual trajectories and are shown in grey. See Supplementary Table 1 for fitted TAMSD values. **c**, Histograms showing probability density of average step size of each crystal over normalized time. Maroon bins show overlapping data in probability distributions. Solid curve is the step-size distribution predicted by our model of propulsive activity due to H_2O_2 catalysis. **d**, TAMSD of hemozoin crystals in expanded FVs compared to particles simulated with Brownian motion trajectories, experimental interaction potentials, confinement derivation from diagram in Fig. 4a and distribution of step sizes from Fig. 4c. See Supplementary Table 8 for fitted TAMSD values. Error bars represent the standard deviation of the means of individual trajectories and are shown in grey. **e**, Population analysis of time-averaged mean squared pixel intensity change (TAMSI) of a FV in the specified conditions. Statistical analysis was done by Student's t-test to determine p-values. **f**, Scheme depicting both stimulation and micro-confinement to explain hemozoin crystal trajectories in the FV. Inset: Pink compartments depict possible vesicle remnants within the FV matrix that confine hemozoin motion.

Discussion

Hemozoin formation is both an essential survival mechanism and critical axis of drug activity against blood-stage malaria parasites. Although major structural properties of hemozoin are well studied, the rapid tumbling of these crystals within the parasite FV has remained a major enigma. Our study incisively unravels the origin of this motion, which is both faster than diffusion and subject to surprisingly tight physical constraints that confine crystals to regions that are smaller than FV boundaries (**Fig. 4f**). Quantitative analysis of hemozoin movement thus provides a novel probe into structural obstacles within the FV matrix that may reflect membrane remnants of hemoglobin-uptake vesicles or other heterogeneities related to recent biophysical observations in yeast cytoplasm.[42] While the static nature of the *P. falciparum* FV has been visualized extensively by electron microscopy, the dynamic biophysical properties of this environment have remained inaccessible until now.

Our results support the biological paradigm that metal-catalyzed H_2O_2 decomposition on the surfaces of hemozoin generates a random propulsive force to boost crystals towards larger steps that enhance diffusion while maintaining an unpredictable trajectory. This propulsive chemical mechanism is well-documented for synthetic metallic nanomachines, but *Plasmodium* hemozoin provides an unprecedented biochemical example of such nanoparticle self-propulsion in cells.[38,39] Additional biological phenomena with this mechanism are likely to exist. Peroxide decomposition is expected to contribute to detoxification of abundant H_2O_2 generated within the FV during large-scale RBC hemoglobin digestion. Chemical strategies that interfere with hydrogen peroxide decomposition are therefore predicted to increase oxidative stress for parasites and consequently sensitize them to therapeutic strategies that target this vacuole.

Main Text References

1 Venkatesan, P. The 2023 WHO World malaria report. *Lancet Microbe* **5**, e214-e214 (2024). https://doi.org:10.1016/S2666-5247(24)00016-8

2 Matz, J. M. Plasmodium's bottomless pit: properties and functions of the malaria parasite's digestive vacuole. *Trends Parasitol* **38**, 525-543 (2022). https://doi.org:10.1016/j.pt.2022.02.010

3 Pagola, S., Stephens, P. W., Bohle, D. S., Kosar, A. D. & Madsen, S. K. The structure of malaria pigment beta-haematin. *Nature* **404**, 307-310 (2000). https://doi.org:10.1038/35005132

4 Noland, G. S., Briones, N. & Sullivan, D. J., Jr. The shape and size of hemozoin crystals distinguishes diverse Plasmodium species. *Mol Biochem Parasitol* **130**, 91-99 (2003). https://doi.org:10.1016/s0166-6851(03)00163-4

5 Sullivan, D. J., Jr., Gluzman, I. Y., Russell, D. G. & Goldberg, D. E. On the molecular mechanism of chloroquine's antimalarial action. *Proc Natl Acad Sci U S A* **93**, 11865-11870 (1996). https://doi.org:10.1073/pnas.93.21.11865

6 Tilley, L., Straimer, J., Gnadig, N. F., Ralph, S. A. & Fidock, D. A. Artemisinin Action and Resistance in Plasmodium falciparum. *Trends Parasitol* **32**, 682-696 (2016). https://doi.org:10.1016/j.pt.2016.05.010

7 Wongtanachai, J., Silamut, K., Day, N. P., Dondorp, A. & Chaisri, U. Effects of antimalarial drugs on movement of Plasmodium falciparum. *Southeast Asian J Trop Med Public Health* **43**, 1-9 (2012).

8 Sachanonta, N. *et al.* Ultrastructural and real-time microscopic changes in P. falciparum-infected red blood cells following treatment with antimalarial drugs. *Ultrastruct Pathol* **35**, 214-225 (2011). https://doi.org:10.3109/01913123.2011.601405

9 Matz, J. M. *et al.* A lipocalin mediates unidirectional heme biomineralization in malaria parasites. *Proc Natl Acad Sci U S A* **117**, 16546-16556 (2020). https://doi.org:10.1073/pnas.2001153117

10 Burda, P. C. *et al.* Structure-Based Identification and Functional Characterization of a Lipocalin in the Malaria Parasite Plasmodium falciparum. *Cell Rep* **31**, 107817 (2020). https://doi.org:10.1016/j.celrep.2020.107817

11 Sigala, P. A., Crowley, J. R., Henderson, J. P. & Goldberg, D. E. Deconvoluting heme biosynthesis to target blood-stage malaria parasites. *Elife* **4** (2015). https://doi.org:10.7554/eLife.09143

12 Hao, S. J., Hou, J. F., Jiang, N. & Zhang, G. J. Loss of membrane cholesterol affects lysosomal osmotic stability. *Gen Physiol Biophys* **27**, 278-283 (2008).

13 Yang, L., Zhang, G. J., Zhong, Y. G. & Zheng, Y. Z. Influence of membrane fluidity modifiers on lysosomal osmotic sensitivity. *Cell Biol Int* **24**, 699-704 (2000). https://doi.org:10.1006/cbir.2000.0552

14 Hu, M., Zhou, N., Cai, W. & Xu, H. Lysosomal solute and water transport. *J Cell Biol* **221** (2022). https://doi.org:10.1083/jcb.202109133

15 Brown, F. R. S. H. M. R. S. E. R. I. A. V. P. L. S. R. XXVII. A brief account of microscopical observations made in the months of June, July and August 1827, on the particles contained in the pollen of plants; and on the general existence of active molecules in organic and inorganic bodies. *Philosophical Magazine Series 2* **4:21** (1828). https://doi.org:10.1080/14786442808674769

16 Einstein, A. Über die von der molekularkinetischen Theorie der Wärme geforderte Bewegung von in ruhenden Flüssigkeiten suspendierten Teilchen. *Annalen der Physik* **322**, 549-560 (1905). https://doi.org:10.1002/andp.19053220806

17 Sutherland, W. A dynamical theory of diffusion for non-electrolytes and the molecular mass of albumin. *The London, Edinburgh, and Dublin Philosophical Magazine and Journal of Science* **9:54**, 781-785 (1905). https://doi.org:10.1080/14786440509463331

18 Smoluchowski, M. v. Zur kinetischen Theorie der Brownschen Molekularbewegung und der Suspensionen. *Annalen der Physik* **326**, 756-780 (1906). https://doi.org:10.102/andp.19063261405

19 Richardson, L. F. Atmospheric diffusion shown on a distance-neighbour graph. *P R Soc Lond a-Conta* **110**, 709-737 (1926). https://doi.org:DOI 10.1098/rspa.1926.0043

20 Liu, T. *et al.* Quantitatively mapping cellular viscosity with detailed organelle information via a designed PET fluorescent probe. *Sci Rep* **4**, 5418 (2014). https://doi.org:10.1038/srep05418

21 Kuimova, M. K. Mapping viscosity in cells using molecular rotors. *Phys Chem Chem Phys* **14**, 12671-12686 (2012). https://doi.org:10.1039/c2cp41674c

22 Devany, J., Chakraborty, K. & Krishnan, Y. Subcellular Nanorheology Reveals Lysosomal Viscosity as a Reporter for Lysosomal Storage Diseases. *Nano Lett* **18**, 1351-1359 (2018). https://doi.org:10.1021/acs.nanolett.7b05040

23 Su, D., Teoh, C. L., Gao, N., Xu, Q. H. & Chang, Y. T. A Simple BODIPY-Based Viscosity Probe for Imaging of Cellular Viscosity in Live Cells. *Sensors (Basel)* **16** (2016). https://doi.org:10.3390/s16091397

24 Abbe, E. Archiv für Mikroskopische Anat Entwicklungsmech. **9**, 413-468 (1873).

25 Huber, G. A. & McCammon, J. A. Brownian Dynamics Simulations of Biological Molecules. *Trends Chem* **1**, 727-738 (2019). https://doi.org:10.1016/j.trechm.2019.07.008

26 Noid, W. G. Perspective: Coarse-grained models for biomolecular systems. *J Chem Phys* **139**, 090901 (2013). https://doi.org:10.1063/1.4818908

27 Weber, S. C., Thompson, M. A., Moerner, W. E., Spakowitz, A. J. & Theriot, J. A. Analytical Tools To Distinguish the Effects of Localization Error, Confinement, and Medium Elasticity on the Velocity Autocorrelation Function. *Biophysical Journal* **102**, 2443-2450 (2012). https://doi.org:10.1016/j.bpj.2012.03.062

28 Kapishnikov, S. *et al.* Oriented nucleation of hemozoin at the digestive vacuole membrane in Plasmodium falciparum. *Proc Natl Acad Sci U S A* **109**, 11188-11193 (2012). https://doi.org:10.1073/pnas.1118120109

29 Weiss, M., Elsner, M., Kartberg, F. & Nilsson, T. Anomalous subdiffusion is a measure for cytoplasmic crowding in living cells. *Biophys J* **87**, 3518-3524 (2004). https://doi.org:10.1529/biophysj.104.044263

30 Alder, A. *et al.* The role of Plasmodium V-ATPase in vacuolar physiology and antimalarial drug uptake. *Proc Natl Acad Sci U S A* **120**, e2306420120 (2023). https://doi.org:10.1073/pnas.2306420120

31 Francis, S. E., Sullivan, D. J., Jr. & Goldberg, D. E. Hemoglobin metabolism in the malaria parasite Plasmodium falciparum. *Annu Rev Microbiol* **51**, 97-123 (1997). https://doi.org:10.1146/annurev.micro.51.1.97

32 Atamna, H. & Ginsburg, H. Origin of reactive oxygen species in erythrocytes infected with Plasmodium falciparum. *Mol Biochem Parasitol* **61**, 231-241 (1993). https://doi.org:10.1016/0166-6851(93)90069-a

33 Ma, X. *et al.* Reversed Janus Micro/Nanomotors with Internal Chemical Engine. *ACS Nano* **10**, 8751-8759 (2016). https://doi.org:10.1021/acsnano.6b04358

34 Wang, Y. *et al.* Bipolar electrochemical mechanism for the propulsion of catalytic nanomotors in hydrogen peroxide solutions. *Langmuir* **22**, 10451-10456 (2006). https://doi.org:10.1021/la0615950

35 Hitt, D. L., Zakrzwski, C. M. & Thomas, M. A. MEMS-based satellite micropropulsion via catalyzed hydrogen peroxide decomposition. *Smart Mater Struct* **10**, 1163-1175 (2001). https://doi.org:Doi 10.1088/0964-1726/10/6/305

36 Eloul, S., Poon, W. C. K., Farago, O. & Frenkel, D. Reactive Momentum Transfer Contributes to the Self-Propulsion of Janus Particles. *Physical Review Letters* **124** (2020). https://doi.org:ARTN 188001
10.1103/PhysRevLett.124.188001

37 Bechinger, C. *et al.* Active Particles in Complex and Crowded Environments. *Rev Mod Phys* **88** (2016). https://doi.org:ARTN 45006
10.1103/RevModPhys.88.045006

38 Howse, J. R. *et al.* Self-motile colloidal particles: From directed propulsion to random walk. *Physical Review Letters* **99** (2007). https://doi.org:ARTN 048102
10.1103/PhysRevLett.99.048102

39 Golestanian, R., Liverpool, T. B. & Ajdari, A. Propulsion of a molecular machine by asymmetric distribution of reaction products. *Phys Rev Lett* **94**, 220801 (2005). https://doi.org:10.1103/PhysRevLett.94.220801

40 Becker, K. *et al.* Oxidative stress in malaria parasite-infected erythrocytes: host-parasite interactions. *Int J Parasitol* **34**, 163-189 (2004). https://doi.org:10.1016/j.ijpara.2003.09.011

41 Basco, L. K. Cultivation of Asexual Intraerythrocytic Stages of Plasmodium falciparum. *Pathogens* **12** (2023). https://doi.org:10.3390/pathogens12070900

42 Garner, R. M., Molines, A. T., Theriot, J. A. & Chang, F. Vast heterogeneity in cytoplasmic diffusion rates revealed by nanorheology and Doppelganger simulations. *Biophys J* **122**, 767-783 (2023). https://doi.org:10.1016/j.bpj.2023.01.040

Supplementary Tables

Table 1. Results of fitting anomalous and normal diffusion models to single-particle tracking TAMSD data with static localization error correction. Error bars based on curve fitting, as described in Methods. For σ, values without parentheses indicate fit to the anomalous model ($4\Gamma t^{\alpha}+\sigma$) while values inside parentheses indicate fit to the linear model ($4Dt+\sigma$).

	α	Γ ($\mu m^2/s^{\alpha}$)	D ($\mu m^2/s$)	σ (μm^2)
hemozoin in 15% peroxide (all) from 0.1 s to 0.4 s	1.03±0.09	2.09±0.14	2.04±0.04	0.03±0.13 (0.00±0.02)
hemozoin in water (all) from 0.1 s to 0.4 s	0.97±0.06	1.06±0.04	1.079±0.014	0.00±0.05 (0.024±0.009)
hemozoin in 40% glycerol (all) from 0.1 s to 0.4 s	1.04±0.08	0.269±0.015	0.261±0.004	0.039±0.014 (0.031±0.004)
hemozoin in 60% glycerol (all) from 0.1 s to 0.4 s	1.04±0.08	0.102±0.006	0.0991±0.0015	0.026±0.006 (0.0232±0.0011)

hemozoin in food vacuole (length≤300) from 0.1 s to 0.4 s	0.64±0.12 1.8mW/cm^2: 0.6±0.2 11.2mW/cm^2: 0.7±0.2 25.3mW/cm^2: 0.6±0.2	0.173±0.004 1.8mW/cm^2: 0.159±0.007 11.2mW/cm^2: 0.164±0.007 25.3mW/cm^2: 0.144±0.006	0.200±0.004 1.8mW/cm^2: 0.185±0.008 11.2mW/cm^2: 0.189±0.006 25.3mW/cm^2: 0.166±0.006	0.00±0.04 (0.082±0.003) 1.8mW/cm^2: 0.00±0.08 (0.083±0.006) 11.2mW/cm^2: 0.00±0.05 (0.071±0.004) 25.3mW/cm^2: 0.00±0.07 (0.087±0.004)

Table 2. Results of fitting normal and anomalous diffusion models to single-particle tracking TAM[SD/Δt] *data with static localization error correction, where i is time lag. Error bars based on curve fitting, as described in Methods. For* σ*, values without parentheses indicate fit to the anomalous model (*$4\Gamma i^{\alpha}+s$*) while values inside parentheses indicate fit to the linear model (*$4Di+s$*).*

	α	Γ (μm^2/s$^\alpha$)	D (μm^2/s)	*s* (μm^2/s)
hemozoin in 15% peroxide (all) from 30 to	1.00±0.07	2.0±0.8	1.96±0.03	10±30 (11±6)

140				
hemozoin in water (all) from 30 to 140	1.02±0.05	1.0±0.2	1.117±0.012	10±12 (7±2)
hemozoin in 40% glycerol (all) from 30 to 140	0.99±0.06	0.27±0.09	0.262±0.004	11±4 (11.3±0.8)
hemozoin in 60% glycerol (all) from 30 to 140	1.01±0.06	0.10±0.03	0.1017±0.0014	8±2 (7.6±0.3)

Table 3. Results of fitting anomalous and normal diffusion models to single-particle tracking TAMSD data with static localization error correction. Error bars based on curve fitting, as described in Methods. For σ, values without parentheses indicate fit to the anomalous model ($4\Gamma t^{\alpha}+\sigma$) while values inside parentheses indicate fit to the linear model ($4Dt+\sigma$).

	α	Γ ($\mu m^2/s^{\alpha}$)	D ($\mu m^2/s$)	σ (μm^2)
nanobeads in	1.01±0.12	0.56±0.04	0.554±0.012	0.00±0.05

peroxide (all) from 0.1 s to 0.4 s				(0.000±0.008)
nanobeads in water (all) from 0.1 s to 0.4 s	1.10±0.12	0.54±0.05	0.507±0.012	0.04±0.04 (0.007±0.008)
nanobeads in 40% glycerol (all) from 0.1 s to 0.4 s	1.01±0.03	0.134±0.003	0.1332±0.0008	0.003±0.003 (0.0022±0.0006)
nanobeads in 60% glycerol (all) from 0.1 s to 0.4 s	0.98±0.02	0.0254±0.0003	0.02572±0.00010	0.017±0.006 (0.00109±0.00007)

Table 4. Results of fitting normal and anomalous diffusion models to single-particle tracking $\mathrm{TAM}[\mathrm{SD}/\Delta t]$ *data with static localization error fitted, where i is time lag. Error bars based on curve fitting, as described in Methods. For* σ, *values without parentheses indicate fit to the anomalous model* ($4\Gamma i^{\alpha}+s$) *while values inside parentheses indicate fit to the linear model* ($4Di+s$).

	α	Γ ($\mu m^2/s^\alpha$)	D ($\mu m^2/s$)	s ($\mu m^2/s$)
nanobeads in peroxide (all) from 13 to 60	1.01±0.09	0.5±0.2	0.555±0.011	0±5 (0±1)
nanobeads in water (all) from 13 to 60	1.05±0.09	0.4±0.2	0.512±0.010	4±5 (1.2±1.0)
nanobeads in 40% glycerol (all) from 30 to 140	1.00±0.02	0.13±0.02	0.1336±0.0007	0.5±0.7 (0.54±0.14)
nanobeads in 60% glycerol (all) from 30 to 140	0.98±0.02	0.028±0.002	0.02529±0.00009	0.24±0.11 (0.38±0.02)

Table 5. Results of fitting unimodal and bimodal diffusion models to single-particle tracking jump length distribution data, where i is time lag.

	D ($\mu m^2/s$)

hemozoin in 15% peroxide (all)	i=1: 2.8±0.2 (D_1) i=1: 38±6%: 0.9±0.2 (D_2) i=1: 62±6%: 5.8±0.9
hemozoin in water (all)	i=1: 1.44±0.08
hemozoin in 40% glycerol (all)	i=1: 0.66±0.04
hemozoin in 60% glycerol (all)	i=10: 0.174±0.006
hemozoin in food vacuole (len<=300)	i=10: 0.37±0.02 (D_1) i=10: 33±2%: 0.132±0.009 (D_2) i=10: 67±2%: 0.63±0.03

Table 6. Parameters of Brownian dynamics simulations using hemozoin-like bricks or spheres. Green highlighted boxes show physical parameters of experimental expanded vacuoles.

	# of particles	Radius (µm)	Viscosity (cP)
Expanded FV 1 (experimental)	35	3	*
Expanded FV 2 (experimental)	23	2.35	*

Expanded FV 3 (experimental)	12	2.3	*
Expanded FV 4 (experimental)	16	1.9	*
Expanded FV 5 (experimental)	19	2.4	*
Expanded FV 6 (experimental)	11	1.95	*
Expanded FV 1 (brick simulation)	35	3	60% glycerol: 10.82 Water: 1
Expanded FV 2 (brick simulation)	23	2.35	60% glycerol: 10.82 Water: 1
Expanded FV 3 (brick simulation)	12	2.3	60% glycerol: 10.82 Water: 1
Expanded FV 4 (brick simulation)	16	1.9	60% glycerol: 10.82 Water: 1
Expanded FV 5 (brick simulation)	19	2.4	60% glycerol: 10.82 Water: 1
Expanded FV 6	11	1.95	60% glycerol: 10.82

(brick simulation)			Water: 1
Expanded FV (sphere simulation)	40	2.9	60% glycerol: 10.82 40% glycerol: 3.72 Water: 1

* experimental condition, undefined viscosity

Table 7. Results of fitting anomalous and normal diffusion models to TAMSD data obtained via Brownian dynamics simulations of hemozoin under confinement.

	α	Γ ($\mu m^2/s^\alpha$)	D ($\mu m^2/s$)
hemozoin in water (all) from 0.1 s to 0.4 s	0.854±0.010	0.704±0.011	0.873±0.003
hemozoin in 60% glycerol (all) from 0.1 s to 0.4 s	0.981±0.010	0.0947±0.0015	0.0976±0.0006

Table 8. Results of fitting anomalous and normal diffusion models to TAMSD data obtained via Brownian dynamics simulations of spheres under confinement.

	α	Γ ($\mu m^2/s^\alpha$)	D ($\mu m^2/s$)
Yukawa-interacting spheres in food vacuole of water viscosity from 0.1 s to 0.4 s	0.90±0.02	0.88±0.03	1.067±0.010
WCA-interacting spheres in food vacuole of water viscosity from 0.1 s to 0.4 s	0.90±0.02	0.82±0.04	1.004±0.009
LJ-interacting spheres in food vacuole of water viscosity from 0.1 s to 0.4 s	0.89±0.02	0.83±0.03	1.019±0.009
Yukawa-interacting spheres in food vacuole of 3.72 * water viscosity from 0.1 s to 0.4 s	0.93±0.02	0.272±0.010	0.310±0.002

WCA-interacting spheres in food vacuole of 3.72 * water viscosity from 0.1 s to 0.4 s	0.93±0.02	0.266±0.010	0.302±0.003
LJ-interacting spheres in food vacuole of 3.72 * water viscosity from 0.1 s to 0.4 s	0.96±0.02	0.275±0.011	0.300±0.003
Noninteracting spheres in food vacuole (R = 2.9 μm) of 10.82 * water viscosity WITH PEROXIDE BOOST from 0.1 s to 0.4 s	0.94±0.03	0.309±0.012	0.333±0.002
Noninteracting spheres in food vacuole (R = 1.2 μm) of 10.82 * water	0.78±0.03	0.188±0.006	0.250±0.002

viscosity WITH PEROXIDE BOOST from 0.1 s to 0.4 s			
Noninteracting spheres in food vacuole (R = 1.1 μm) of 10.82 * water viscosity WITH PEROXIDE BOOST from 0.1 s to 0.4 s	0.71±0.02	0.163±0.006	0.236±0.002
Yukawa-interacting spheres in food vacuole of 10.82 * water viscosity from 0.1 s to 0.4 s	0.97±0.02	0.106±0.004	0.1110±0.0009
WCA-interacting spheres in food vacuole of 10.82 * water viscosity from 0.1 s to 0.4 s	0.97±0.02	0.103±0.004	0.1090±0.0009
LJ-interacting	0.95±0.02	0.099±0.003	0.1085±0.0008

spheres in food vacuole of 10.82 * water viscosity from 0.1 s to 0.4 s			

Supplementary Video 1 *P. falciparum*-infected human RBC. This video shows hemozoin tumbling from Extended Data Fig. 1a. Hemozoin crystals are tumbling within the singular food vacuole (FV) compartment inside a parasite that has infected a red blood cell (RBC). Total elapsed time: 5 s. Total frame area is 8.3µm x 8.3µm

Supplementary Video 2 *P. falciparum*-infected human RBC that was lethally-dosed with 0.1µM chloroquine (see Methods). This video shows static hemozoin crystals from Extended Data Fig. 1a. Total elapsed time: 5 s. Total frame area is 11.8µm x 11.3µm.

Supplementary Video 3 *P. falciparum*-infected human RBC used in TAMSI analysis. This video shows moving hemozoin in the FV that is quantified for TAMSI in Extended Data Fig. 2a. Total elapsed time: 5 s. Total frame area is 10.8µm x 9.8µm.

Supplementary Video 4 Expanded FV after hypotonically treating parasites for 20 min. This video shows tumbling crystals that have enough space to spread out after FV expansion. Total elapsed time: 10 s. Total frame area is 8.0µm x 7.2µm

Supplementary Video 5 Simulation of 35 cuboidal particles confined in a 3µm radius spherical boundary with a viscosity of 10 cP. This video shows the Brownian dynamics of simulated hemozoin crystals in a crowded environment with the repulsive term of the Lennard-Jones potential to enforce volume-exclusion between particles. Total elapsed time: 5 s. X-, y- and z-planes are measured in m.

Supplementary Video 6 Simulation of 40 spheres in 2.9µm radius spherical boundary with a viscosity of 10 cP. This video shows the Brownian dynamics of simulated spheres in a crowded environment with interaction potentials mimicking experimental potentials via the Direct Boltzmann Inversion method. Total elapsed time: 20 s. X-, y-, and z-planes are measured in µm.

Methods

Cell culture

Parasite culturing

P. falciparum Dd2[42] and NF54[43] parasites were grown in human red blood cells received from the University of Utah Hospital blood bank at 90% N_2, 5% CO_2, and 5% O_2 at 37°C in RPMI 1640 containing AlbuMAXI (Thermo Fisher Scientific) supplemented with glutamine (2% hematocrit), as previously described.[44] Medium was changed daily. Parasitemia was measured by Giemsa-stained blood smear or by flow cytometry.[44] Parasites were routinely synchronized to the early ring stage by treatment with 5% D-sorbitol. All imaging of hemozoin motion was performed using late trophozoite- and schizont-stage parasites (36-48 hours post synchronization).

Parasite fractionation

Intact parasites within a permeabilized RBC ghost and isolated food vacuoles were prepared by membrane lysis. Parasitized red blood cells were permeabilized with 0.05% saponin in PBS, as described previously.[44] This treatment released the hemoglobin contents in the RBC but maintained the membrane of isolated intact parasites. The plasma membrane of isolated parasites was permeabilized with exposure to ice-cold acidic hypotonic buffer (20 mM MES, pH 4.5), transferred to a watch glass on ice, mixed forcefully through a 27-G needle, and centrifuged at 15,800xg. The supernatant was removed by vacuum aspiration, and the pellet was resuspended in intracellular solution (120 mM KCl, 10 mM NaCl, 25 mM HEPES, 2 mM $MgCl_2$, 5 mM Na_2HPO_4, pH 7.3) and triturated with a 27-G needle, as previously described.[45] Isolated food vacuoles were resuspended on ice and imaged within 20 mins of isolation.

Inhibitor treatments

Parasites were magnet purified (isolating schizont stages) and incubated for 6 hours with fresh red blood cells. Newly invaded red blood cells were treated with 5% D-sorbitol (isolating ring stages) to produce rings with a 6-hour synchrony window. Parasites were separated into different wells and treated with high concentrations of inhibitors to induce cell death. Parasites were treated continuously with 0.2 µM WR99210 after ring synchronization (IC_{50}: 0.043 µM); 0.1 µM chloroquine at 30 hours post-synchronization (IC_{50}: 0.024 µM); 0.2 µM artemisinin at 30 hours post synchronization (IC_{50}: 0.032 µM); or 200 µM ALA at 24 hours post synchronization followed by 1 min of light exposure after 12 hours of ALA incubation.[11,46] Parasites were imaged at 36 hours post-synchronization and were scored based on moving vs. not moving hemozoin crystals. Thirty parasites were counted for each replicate and three replicates were taken for each drug treatment. Image analysis and TAMSI quantification was performed on chloroquine-treated parasites, although similar results were obtained for all drug-treatment conditions.

Microscopy

Widefield microscopy

Live parasites were imaged with a Nikon Ti-E inverted widefield microscope equipped with an Andor Zyla CMOS camera and 100X PlanAPO oil immersion objective. All pixel analysis time lapses were taken at ≥300 fps, while all single-particle tracking time lapses were taken ≥200 fps (slower frame rate due to larger region of interest). Microscope slides were incubated for 5 mins of “rest” after sample mounting and before imaging to minimize drift/bulk fluid flows under the microscope. All time lapse images were compiled as .nd2 files. Samples containing infected RBCs at 12-15% trophozoite or schizont parasitemia were mounted on a standard 75 x 25-mm glass microscope slide. For imaging, 7 µL of the resuspended culture was deposited on a slide and covered with a 22 x 40-mm coverslip. Even pressure was applied to the sample to remove excess liquid and the coverslip was sealed with clear nail polish to prevent evaporation. Low oxygen condition samples were imaged with flat-bottom dishes (CellTreat, #229632) on the same microscope, to ensure a sealed incubator that maintained low oxygen concentrations

Low O_2 environment

An OKOLAB stage incubator on the Nikon Ti-E microscope was used with a dish adaptor. The clear lid was sealed with parafilm and flushed with CO_2 for 20 minutes before images were collected. Samples were measured by an FD-103 Waterproof and Shockproof O_2 Meter (Forensics

Detectors) with a tube connection to the sealed incubator. Meter had range between 0-30% O_2 with resolution within 0.1% O_2 within < 1 minute.

Expanded vacuoles

Infected red blood cells were incubated in 100 µl of media diluted 1:1 with deionized water at 37°C for 20 mins before imaging. For imaging, 7 µL was deposited on a slide and sealed with a coverslip. Expanded vacuoles that retained hemozoin motion were imaged as described above.

Hemozoin isolation

A culture of infected RBCs at 1-20% parasitemia was saponin treated and resuspended in cold PBS. Parasites were spun down at 15,000xg for 5 mins, and resuspended in 2% SDS. Crystals were centrifuged at 15,000xg for 5 mins and resuspended in room temperature PBS with 2 µl of Qiagen protease and incubated for an hour at 37°C. Crystals were then washed with 2% SDS and spun at 15,000xg for 5 mins. Crystals were finally resuspended in 6M urea and stored in 4°C until imaging. Crystal pellets were washed twice and resuspended by vortexing in 100% water or 40-60% glycerol/water (w/v) concentrations for imaging.

H_2O_2 addition

30% H_2O_2 (Fisher, BP2633-500) was removed from a freshly opened bottle and mixed 1:1 with an equal volume of hemozoin crystals or nanobeads resuspended in water to give a final concentration of 15% H_2O_2 and immediately mounted onto a microscope slide. The viscosity of 30% H_2O_2 is 1.25 cP, which after mixing with water results in a final effective viscosity of 1.12 cP.[47]

Light intensity

Light intensity on the Nikon Ti-E inverted widefield microscope was measured by a power meter sensor placed in the sample focal plane with a ThorLabs PM100A power meter analog console. Intensity was adjusted by with Sola automated LED lightsource.

Glycerol ratios and viscosity calculations

100% glycerol was added by weight converted to volume to distilled water to make aqueous glycerol solutions at room temperature (w/v). Solutions were vortexed for ≥ 1 hour to ensure adequate mixing. Viscosities were calculated from the simple Stokes-Einstein equation:

$$D = \frac{k_B T}{6\pi\eta r}$$

Where D is the diffusion coefficient derived from temperature (T), Boltzmann constant (k_B), viscosity of surrounding medium (η) and the hydrodynamic radius of the particle (r). Viscosity values were solved by single-particle tracking control nanobeads with defined radius 0.4 µm at room temperature (22°C) and then computing and fitting the time-averaged mean squared displacement (TAMSD):

$$\mathrm{TAMSD}(t) = 4Dt + \sigma$$

Where t is elapsed time. This model accounts for static localization error inherent to SPT data by introducing constant factor σ.[27] Experimentally determined viscosities for nanobeads in the respective glycerol concentrations were nearly identical to literature values for these conditions.[48] The effective viscosity from hypotonic expansion of vacuoles was estimated by using a weighted average:

$$\text{Average viscosity of expanded vacuole} = \frac{x_1 w_1 + x_2 w_2}{w_1 + w_2}$$

Where x is the estimated or calculated viscosity and w is percent of total expanded volume with that expected viscosity. We estimated wild type food vacuoles had viscosities similar to lysosomes (100 – 400 cP) and that the increase in volume from swelling was due solely to the influx of water (1 cP). We estimated that 90% of the swollen volume was water with 10% of the final volume having the original 100 cP lysosome viscosity, creating an effective 10 cP viscosity for the expanded vacuole.

Image analysis

Time-averaged mean squared pixel change intensity (TAMSI)

Single-particle tracking (SPT) proved challenging due to crystal congestion and overlapping trajectories within the small volume of the FV, limiting tracking to only a few frames. To overcome these limitations, we introduced a new metric to assess crystal mobility: the time-averaged mean squared pixel intensity change (TAMSI) within the FV area as a function of elapsed time. Beyond approximately 0.2 s, TAMSI reached a plateau, indicating that crystal movement had fully decorrelated and longer elapsed times no longer contributed to increased pixel intensity changes. We empirically fit this time-dependent change to a power law growth function to determine the average characteristic time at which 50% of the plateau value was reached (see *Fitting* Methods section):

$$< [\Delta I(t)]^2 >= C(1 - \frac{1}{(t/\tau_0)^{\alpha} + 1})$$

This analysis allowed us to define an apparent pixel velocity by dividing the TAMSI by the average characteristic time of ~0.18 s, which we observed in native, living parasites. To compare between different FV-imaging conditions, we used the ~0.18 s characteristic time to determine the pixel velocity for all time lapse experiments.

Datasets were saved as .nd2 files and processed through MATLAB version R2021a with the Bio-Formats toolbox.[49] Each frame of a dataset was adjusted so that bottom and top 1% pixel intensities were saturated to create better image contrast. The dataset was flipped to return the complement pixel intensities of each frame and the region of interest was defined manually by tracing the outer membrane of the food vacuole discernable in brightfield images. Each pixel intensity change was calculated by:

$$\mathrm{TAMSI(t)} = <[\Delta I(t)]^2> = <[I(\tau+t)-I(\tau)]^2>_\tau$$

Where $I(t)$ stands for pixel intensity, and the angle brackets denote averaging over various τ values and over all pixels. Each squared change was averaged over every pixel in the region of interest for every elapsed time τ and plotted as a function of increasing elapsed time.

Fitting

We observed nonexponential relaxation of pixel intensity change as a function of elapsed time. We used a general power law in the following form:

$$<[\Delta I(t)]^2> = C(1-\frac{1}{(t/\tau_0)^\alpha+1})$$

to empirically fit to the experimental data. The relaxation time τ_0 encodes the time t at which pixel intensity change reaches half of its asymptotic value C to which the function tends in the limit of $t\rightarrow\infty$. We used `scipy.optimize.curve_fit` function in Python to empirically fit our data.[50] For dead parasites, the dominant contribution to pixel intensity fluctuation was the background noise that deviated from the power law equation used for conditions with moving hemozoin. Since we observed noise as the dominant feature, we instead used only the first term of expansion of the power law in Poiseux series (for $\alpha = 0.5$, $C = 0.05$):

$$< [\Delta I(t)]^2 >= 0.05\sqrt{t/\tau_0}$$

Before fitting, we subtracted from the experimental data the short-time average computed between 5th and 15th data points. Then, we performed fitting from the 10th data point onwards, where we observed an extremely slow increase. As the number of particles in a small pixel is governed by Poisson distribution, it depends only on the total intensity divided by the number of pixels. For long times t the Poisson random variables are going to be statistically independent, and in principle C can be predicted from the Skellam distribution properties.[51] Thus, we expected C to be comparable between dead and living parasites. Thus, the choice of α and C were based on the median values observed for the infected red blood cell group.

Single-particle tracking

TrackMate

We used the Fiji plugin TrackMate to single-particle track hemozoin crystals throughout time lapse images.[52,53] We chose the LoG (Laplacian of a Gaussian) detector as our method of localization. This method applies a LoG filter to each image to find local maxima with quadratic fitting for sub-pixel localization. We estimated our object diameter to be 0.6 µm unless tracking the defined 0.8 µm diameter nanobeads. Each time lapse was manually processed by resetting the initial thresholding to rule out background spots. We used the Simple LAP tracker because we assumed there would be no branching tracks (particles were not breaking and reforming). We used 0.5 µm as our linking max distance, 0.5 µm for our gap-closing max distance, and 2 as our gap-closing max frame gap. Tracks were minimally filtered by particle spots that were "stuck" where their displacements did not increase with time.

Time-averaged mean squared displacement

For each system, we recorded numerous tracks of different length (number of time points), and different time resolution (differing from experiment to experiment). To analyze such heterogeneous dataset, we first computed and stored all displacements, i.e., $r(i+j)-r(j);\ i,j \in \mathbb{N}$, and used them as a basis for the subsequent analyses.

To compute time-averaged mean squared displacements (TAMSD), we iterated over the list of displacements, squared them, and averaged ones belonging to equal lag i. To i=1, we attributed a timestep averaged over all experiments belonging to the same system.

To compute uncertainties, we repeated the computation of squared displacements (SD) but limiting the computation only to those displacements which are statistically independent. For instance, for the same particle, r(3)-r(0) is not statistically independent from r(5)-r(2). Therefore, we used only these SDs for which start time j is a multiple of the lag time i. For each lag time i, we stored a list of N_i statistically independent SDs.

Subsequently, for each lag time i, we performed 100 random selections of N_i SD values from the list and used standard deviation of the means of the selected samples as a measure of uncertainty in TAMSD value. If there was only 1 value in the SD list, we attributed infinite uncertainty.

We fit TAMSD with two diffusion models:

Normal:

$$\text{TAMSD}\ (t) = 4Dt + \sigma$$

And anomalous:

$$\text{TAMSD}\ (t) = 4\Gamma t^{\alpha} + \sigma$$

We used the `scipy.optimize.curve_fit` function in `python` to empirically fit the data and provided the uncertainties as inverses of fitting weights. This means that in least squares optimization, the residuals are divided by the uncertainties, making the points with poor statistics weigh less.

We fit only the short-time parts of the TAMSD curves (0.1-0.4 s). To ensure that using averaged timesteps did not distort the results, for the systems in which normal diffusion is expected, we divided all the squared displacements by the timestep:

$$\text{TAM}[\text{SD}/\Delta t]\ (\text{i}) = 4Di + \text{s}$$

This procedure led to very similar values (Supplementary Tables 2 and 4 compared to Supplementary Tables 1 and 3, respectively).

Simulations

Control simulations for TAMSI comparison

We used $1/\tau_0$ as a proxy for the diffusion coefficient. To test the accuracy of this approximated value, we performed a series of point-particle Brownian dynamics simulations in which we computed pixel intensity change using the same protocol as when analyzing experimental data, but instead of computing intensity change we computed the number of particles in each pixel. We observed faster relaxation (smaller τ_0) for particles with higher diffusion coefficients D.

Specifically, we performed Brownian dynamics simulations of 600 noninteracting particles of diffusion coefficients D = 2, 10, 20 $\mu m^2/s$ in a 20 nm × 20 nm × 20 nm box (with periodic boundary conditions) for 10000 steps (dt = 500 ps). Then, we divided the system into 100 2D pixels along X and Y dimensions and quantified the number of particles N in each pixel in time. We calculated:

$$< [\Delta N(t)]^2 >=< [N(\tau + t) - N(\tau)]^2 >_\tau$$

and averaged over the pixels. In agreement with Skellam distribution properties, the plateau occurred at twice the average number of particles in a single pixel, which is 2 × 600 / 100 = 12; τ_0 is the value of time at which pixel particle number fluctuation reaches a value of 6. We observed that τ_0 decreases with increase in diffusion coefficient, making its inverse a valid proxy for diffusivity. See Extended Data Fig. 2d and Extended Data Fig. 6 for results. A similar method was used recently employing a “countoscope” analysis.[54] We noted that the simulations are scale invariant, so rescaling the length unit (in pixel size and diffusion coefficients) leads to the same results.

Brownian dynamics simulations

We performed Brownian dynamics simulations of hemozoin-like cuboidal “bricks” using a 1:1:3.5 ratio rectangular prism with dimensions 170x170x585 nm using custom MATLAB version R2021a code.[55] Nodes were spaced ~80 nm apart to total 74 nodes on the surface of each brick. These nodes had regularized stokeslets applied and summed over the entire brick. We calculated randomized rotational and translational steps based on the Stokes-Einstein equation for spherical particles in low Reynolds number. Timestep was 0.0033 s to match timesteps of experimental time lapses, temperature: 293.15 K. Confinement was realized by defining spherical region of various radii and defining repulsive Lennard-Jones interaction between wall and particles. Particle-particle interactions were defined by the same repulsive Lennard-Jones equation with epsilon estimated from published literature ($\varepsilon = 0.08$ kcal/mol, $\sigma = 57$ nm):[56]

$$V_{LJ}(r;\ \varepsilon, \sigma) = 4\varepsilon[(\sigma/r)^{12}]$$

See Supplementary Table 6 for physical parameters of each simulation, which mimicked experimental expanded FV conditions.

Using a custom MATLAB version R2021a code,[55] we modeled a sphere with radius 0.2 μm undergoing thermal translational and rotational diffusion in water due to Langevin forces. In addition, each sphere had propulsion due to chemical activity modeled by a fixed-body translational and rotational velocity. The propulsive velocities of the population of spheres obeyed normal distributions with mean zero. For rotational propulsive velocity, the normal distribution had a standard deviation of 314 rad/s for all three directional components (x, y, z), which is consistent with tumbling rotation speeds we observe in **Supplementary Video 4** (~ 168 – 419 rad/s). For translational propulsive velocity, a standard deviation of 60 μm/s adequately reproduced the step-size distribution for the active portion of the experimental bimodal distribution for hemozoin in 15% H_2O_2. We simulated 1000 trajectories up to 0.33 s to mimic experimental conditions.

We performed Brownian dynamics simulations of 40 spheres in confinement using LAMMPS software (`fix brownian`).[57] Timestep was 1 μs, total number of steps was 20000000, and temperature: 293.15 K. Friction coefficients corresponding to 0%, 40%, and 60% glycerol were: 1917.0, 7131.0, and 20704.0 g $\text{mol}^{-1}\text{fs}^{-1}$. These friction coefficients translate to a hemozoin dynamic radius of 0.169 µm. Confinement was realized by defining spherical region of radius 2.9 µm and defining a short-range harmonic repulsive interaction between wall and particles ($\epsilon = 0.1$kcal/mol/Å^2, $\sigma = 0.1$µm). Simulations with "peroxide boost" were performed via custom `python` code, using the distribution in step sizes from experimental data and implementing hard spherical boundaries.

Parametrizing experimental crystal-crystal interaction

From tracks of hemozoin in the food vacuole, we computed histograms of distances between the separate crystals P(r). We used the Direct Boltzmann Inversion (DBI) method to parametrize the potentials:[58]

$$V(r) = -k_B T \, ln \, [P(r)/P_{ni}(r)]$$

where $P_{ni}(r)$ is the histogram as if the crystals would not interact at all (ideal gas).

We modeled the geometry underlying experimental data as a 3D sphere projected onto a 2D plane. Thus, to compute $P_{ni}(r)$ we performed a following computation:

1. Random-uniform insertion of 10000 point particles into 3D sphere of radius 2.9 µm
2. Projection of coordinates onto the XY plane.
3. Computing distances between all particle projections.
4. Computing histogram of distances, with 100 bins spanning a range from 0.0 to 6.0 µm.

We fit a 6-12 Lennard Jones potential:

$$V_{LJ}(r;\, \varepsilon, \sigma) = 4\varepsilon[(\sigma/r)^{12} - (\sigma/r)^6]$$

to the resultant DBI potential for distances larger than 0.64 μm (to avoid large errors stemming from fitting to a very steep increase due to excluded volume). Parameters giving best match were: ε = 0.24±0.06 kcal/mol, σ = 0.643±0.008 μm.

To show the robustness of our results to a specific form of the potential, we also performed simulations with two different interaction potentials. First, we used Weeks-Chandler-Andersen (WCA) potential — LJ-based exclusively repulsive potential representing volume exclusion:

$$V_{LJ}(r;\ \varepsilon,\sigma) = 4\varepsilon[(\sigma/r)^{12} - (\sigma/r)^{6}] + \varepsilon \text{ for } r < 2^{1/6}\sigma \text{ and 0 otherwise.}$$

with ε and σ remaining the same as in DBI LJ potential.

Second, we used Yukawa potential — exclusively repulsive potential with long-range repulsion:

$$V_{LJ}(r;\ \varepsilon,\sigma) = Ae^{\kappa r}/r$$

with A = 0.3 kcal/mol·μm, κ = 1 μm^{-1}. Global cutoff was set to 2 μm.

Jump distribution

To extend the analysis, we computed histograms of the displacement lengths divided by i$\Delta\tilde{r} = \Delta r/\sqrt{i\Delta t}$. For a Brownian motion, such histograms are governed by the following probability density function:

$$P(\Delta\tilde{r};\ D) = (2D)^{-1}\Delta\tilde{r}\ exp\,[-(\Delta\tilde{r})^2/4D]d\Delta\tilde{r}$$

This function has a maximum for $\Delta\tilde{r} = \sqrt{2D}$.

For low-viscosity systems, we computed histograms for i=1 to maximize the sample size. For high-viscosity systems, we computed histograms for i=10 to avoid contributions of static localization error to the jump statistics. Static localization errors are inherent to SPT data, especially in high viscosity systems with confinement, where the accuracy between the observable particle position is slightly different than the particle's true position.[27]

We observed that fitting with the theoretical expression gives poor results, especially at high-jump length heavy tails. To quantify these tails, we performed fitting with bimodal model, i.e.:

$$P_2(\Delta\tilde{r};\ D_1, D_2, c) = c(2D_1)^{-1}\Delta\tilde{r}\ exp\left[-(\Delta\tilde{r})^2/4D_1\right]d\Delta\tilde{r} + (1-c)(2D_2)^{-1}\Delta\tilde{r}\ exp\left[-(\Delta\tilde{r})^2/4D_2\right]d\Delta\tilde{r}$$

obtaining much better agreement with the experimental curves.

Data availability

All data described in the manuscript are shown in the figures and provided in Supplementary Information. Supplementary videos are provided in figshare. All time lapses for data from pixel analysis (TAMSI) in Fig. 1b,c,d and Fig. 4e are provided in figshare:

Videos - RBCs. figshare. Dataset. https://doi.org/10.6084/m9.figshare.28719737.v1

Videos - RBCs low O2. figshare. Dataset. https://doi.org/10.6084/m9.figshare.28719716.v1

Videos - Isolated parasites. figshare. Dataset. https://doi.org/10.6084/m9.figshare.28719722.v1

Videos - Isolated FVs. figshare. Dataset. https://doi.org/10.6084/m9.figshare.28719734.v1

Videos - Dead parasites. figshare. Dataset. https://doi.org/10.6084/m9.figshare.28719731.v1

Videos - Expanded vacuoles. figshare. Dataset. https://doi.org/10.6084/m9.figshare.28719719.v1

Supplementary Videos. figshare. Dataset. https://doi.org/10.6084/m9.figshare.28835870.v1

Code availability

Data from time lapses and TAMSI analysis were analyzed with custom code written in MATLAB version R2021a. This code was essential for extracting data points for Fig. 1b,c,d. Additional analysis in Extended Fig. 1c,d used a custom `python` code. ImageJ2 version 2.14.0/1.54f commercial software package was used for single-particle tracking. A custom `python` code was written for weighting and compiling individual single-particle tracks into an overall average TAMSD with uncertainty values and a step-size distribution. Brownian dynamics simulations were written by custom MATLAB codes, `python` codes and LAMMPS. All MATLAB and `python` scripts used for data analysis and simulations, along with default parameters are available in the GitHub repository. All experimental single-particle tracks for step-size distribution and TAMSD analysis are also provided in the GitHub repository. (https://github.com/emhastin/HemozoinMotion.git).

Methods References

42 Ponnudurai, T., Leeuwenberg, A. D. & Meuwissen, J. H. Chloroquine sensitivity of isolates of Plasmodium falciparum adapted to in vitro culture. *Trop Geogr Med* **33**, 50-54 (1981).

43 Falekun, S. *et al.* Divergent acyl carrier protein decouples mitochondrial Fe-S cluster biogenesis from fatty acid synthesis in malaria parasites. *Elife* **10** (2021). https://doi.org:10.7554/eLife.71636

44 Saliba, K. J. *et al.* Acidification of the malaria parasite's digestive vacuole by a H+-ATPase and a H+-pyrophosphatase. *J Biol Chem* **278**, 5605-5612 (2003). https://doi.org:10.1074/jbc.M208648200

45 Sanz, L. M. *et al.* P. falciparum in vitro killing rates allow to discriminate between different antimalarial mode-of-action. *PLoS One* **7**, e30949 (2012). https://doi.org:10.1371/journal.pone.0030949

46 Phibbs, M. K. & Giguere, P. A. Hydrogen peroxide and its analogues. I. Density, refractive index, viscosity, and surface tension of deuterium peroxide-deuterium oxide solutions. *Can J Chem* **29**, 173-181 (1951). https://doi.org:10.1139/v51-022

47 Segur, J. B. & Oberstar, H. E. Viscosity of Glycerol and Its Aqueous Solutions. *Ind Eng Chem* **43**, 2117-2120 (1951). https://doi.org:DOI 10.1021/ie50501a040

48 Tay, J. W. *Bioformats Image Toolbox*, <https://github.com/Biofrontiers-ALMC/bioformats-matlab/releases/tag/v1.2.3)> (2025).

49 Virtanen, P. *et al.* SciPy 1.0: fundamental algorithms for scientific computing in Python. *Nat Methods* **17**, 261-272 (2020). https://doi.org:10.1038/s41592-019-0686-2

50 Skellam, J. G. The Frequency Distribution of the Difference between 2 Poisson Variates Belonging to Different Populations. *J Roy Stat Soc a Sta* **109**, 296-296 (1946). https://doi.org:Doi 10.2307/2981372

51 Ershov, D. *et al.* TrackMate 7: integrating state-of-the-art segmentation algorithms into tracking pipelines. *Nat Methods* **19**, 829-832 (2022). https://doi.org:10.1038/s41592-022-01507-1

52 Tinevez, J. Y. *et al.* TrackMate: An open and extensible platform for single-particle tracking. *Methods* **115**, 80-90 (2017). https://doi.org:10.1016/j.ymeth.2016.09.016

53 Mackay, E. K. R., Marbach, S., Sprinkle, B. & Thorneywork, A. L. The Countoscope: Measuring Self and Collective Dynamics without Trajectories. *Phys Rev X* **14** (2024). https://doi.org:ARTN 041016
10.1103/PhysRevX.14.041016

54 Kapishnikov, S. *et al.* Aligned hemozoin crystals in curved clusters in malarial red blood cells revealed by nanoprobe X-ray Fe fluorescence and diffraction. *Proc Natl Acad Sci U S A* **109**, 11184-11187 (2012). https://doi.org:10.1073/pnas.1118134109

55 Ando, T. & Skolnick, J. Crowding and hydrodynamic interactions likely dominate in vivo macromolecular motion. *Proc Natl Acad Sci U S A* **107**, 18457-18462 (2010). https://doi.org:10.1073/pnas.1011354107

56 Thompson, A. P. *et al.* LAMMPS-a flexible simulation tool for particle-based materials modeling at the atomic, meso, and continuum scales. *Comput Phys Commun* **271** (2022). https://doi.org:ARTN 108171
10.1016/j.cpc.2021.108171

57 Reith, D., Pütz, M. & Müller-Plathe, F. Deriving effective mesoscale potentials from atomistic simulations. *J Comput Chem* **24**, 1624-1636 (2003). https://doi.org:10.1002/jcc.10307

Acknowledgements

We thank Kiarash Samsami, Ludivine Sanchez-Arias, and Sigala lab members for helpful discussions. We thank Xiang Wang, Mike Bridge, and Anton Classen at the Utah Cell Imaging Core Facility; Shawn Colby at the Health Sciences Machine Shop; and Brian Van Devener at the Utah Nanofab for experimental assistance. This work was supported by NIH grants R35GM133764 (PAS), R21AI185746 (PAS), and R35GM147491 (TCB); a pilot award (PAS) from the Utah Center for Iron and Heme Disorders (U54DK110858); and a pilot award jointly funded by the Price College of Engineering and the 3i Initiative at the University of Utah (PAS, HF, and TCB). EMH was funded in part by NIH training grant T32AI055434. Brightfield microscopy and flow cytometry were performed using core facilities at the University of Utah.

Author Contributions

EMH and PAS designed and coordinated the study. EMH performed all experimental assays including parasite culture, microscopy, FV expansion, hemozoin isolation, and peroxide assays. EMH performed all SPT. EMH, KC, and TS scripted image analysis codes. EMH, TS, HF, and TCB scripted simulation codes. EMH and TS analyzed SPT data. EMH, TS, HF, TCB, and PAS interpreted data. EMH, TS, HF, TCB, and PAS wrote and/or edited the manuscript.

Competing Interest Declaration

The authors declare no competing interests.

Additional Information

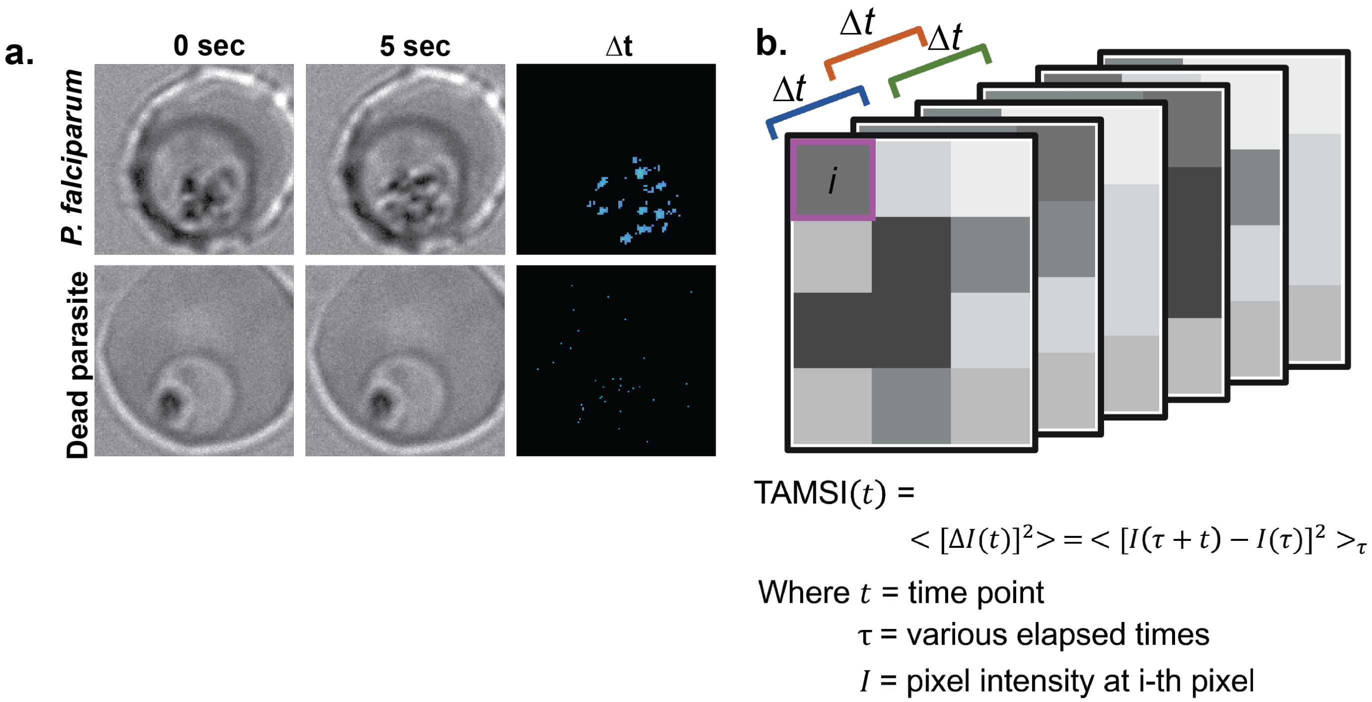

Extended Data Figure 1: Time lapse image analysis of parasite hemozoin motion. a, Live time lapse images of parasite-infected RBCs with pixel-by-pixel subtraction over 5 seconds and heat maps to display biggest pixel differences. **b**, Diagram explaining image analysis where each pixel's intensity is subtracted over consecutive frames and averaged within region of interest to define average squared change over elapsed time.

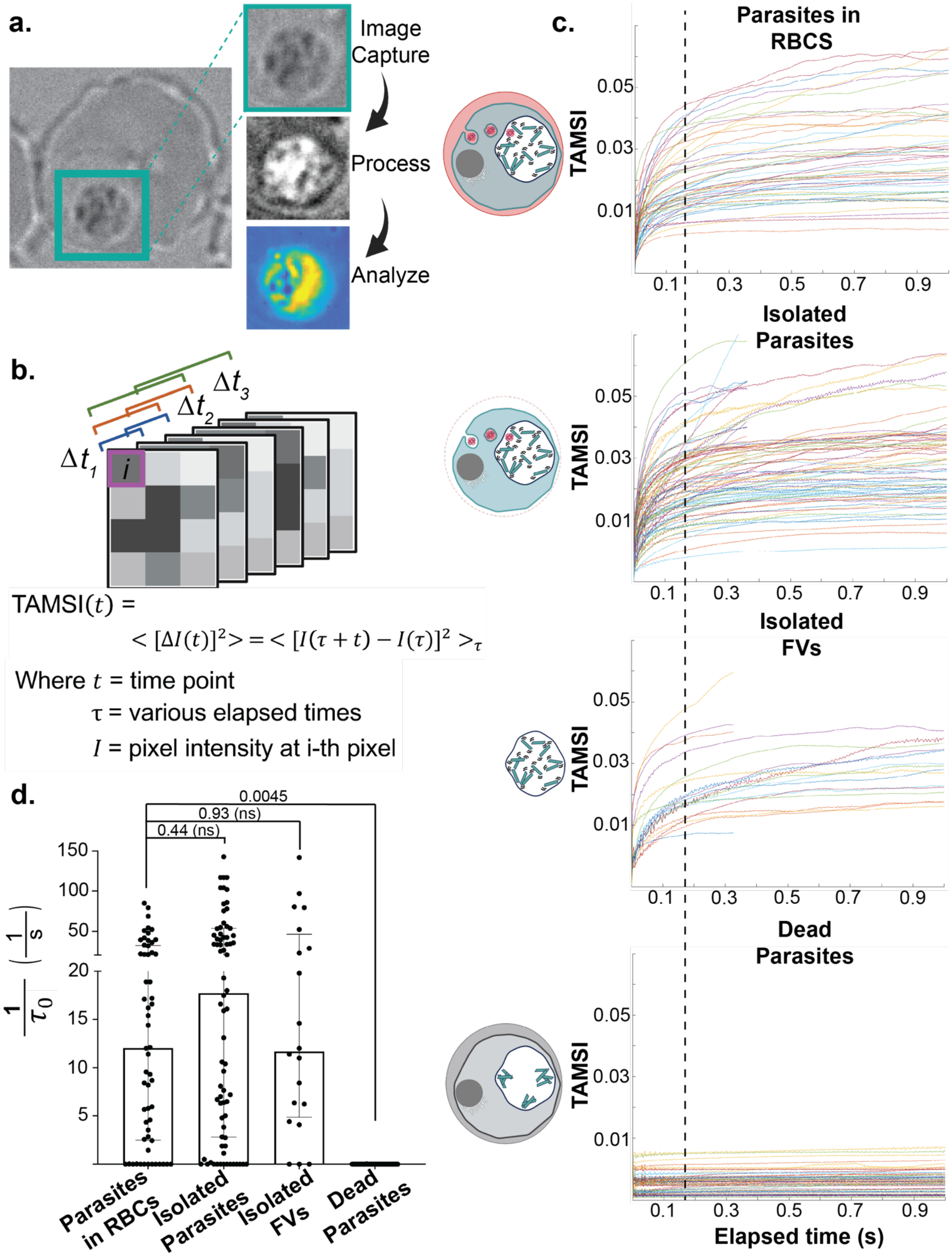
a.
Image Capture
Process
Analyze
b.
Δt_1
Δt_2
Δt_3
i
TAMSI(t) =
$< [\Delta I(t)]^2 > = < [I(\tau + t) - I(\tau)]^2 >_\tau$
Where t = time point
τ = various elapsed times
I = pixel intensity at i-th pixel
c.
Parasites in RBCS
Isolated Parasites
Isolated FVs
Dead Parasites
TAMSI
0.05
0.03
0.01
0.1
0.3
0.5
0.7
0.9
Elapsed time (s)
d.
0.0045
0.93 (ns)
0.44 (ns)
$\frac{1}{\tau_0}$ $\left(\frac{1}{s}\right)$
150
100
50
20
15
10
5
Parasites in RBCs
Isolated Parasites
Isolated FVs
Dead Parasites

Extended Data Figure 2: Fractionation and quantitative analysis of hemozoin motion. a, Example of image analysis method where food vacuole is captured at above frame rate threshold, preprocessed to normalize pixel intensity values, then analyzed with overall pixel intensity change over time. **b**, Diagram explaining image analysis where each pixel's intensity is subtracted over different elapsed times, squared, and averaged within region of interest to define change in progressively longer elapsed times. **c**, Cumulative data from different time lapse experiments indicating a constant elapsed time (~0.18 s) was chosen to determine velocities of all conditions. **d**, A general power law fits experimental data in Extended Data Fig. 2c where $1/\tau_0$ can be used as a proxy for diffusion coefficients. This correlation was corroborated by Brownian dynamics simulations where both TAMSI and diffusion coefficients were calculated for each data set and larger $1/\tau_0$ had a higher diffusion coefficient. See Extended Data Figure 6. Each point indicates $1/\tau_0$ of the same experimental data in Fig. 1b. For dead parasites, only the first term in expansion of the power law in Poiseux series was used. Statistical analysis was done by Student's t-test to determine the indicated p values.

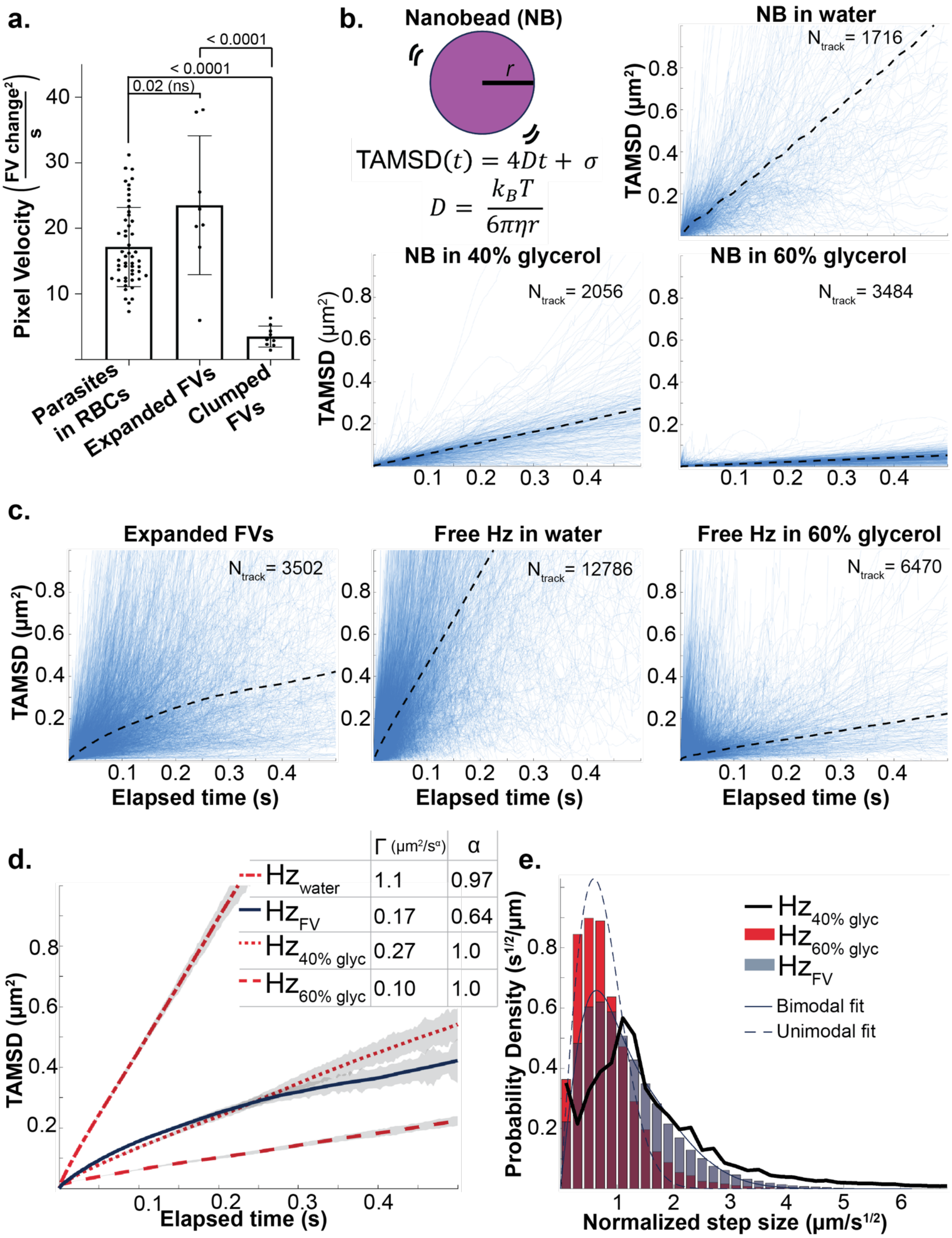
a.
Pixel Velocity (FV change²/s)
< 0.0001
< 0.0001
0.02 (ns)
Parasites in RBCs
Expanded FVs
Clumped FVs
b.
Nanobead (NB)
r
TAMSD(t) = 4Dt + σ
D = k_B T / 6πηr
NB in water
N_track = 1716
NB in 40% glycerol
N_track = 2056
NB in 60% glycerol
N_track = 3484
TAMSD (µm²)
c.
Expanded FVs
N_track = 3502
Free Hz in water
N_track = 12786
Free Hz in 60% glycerol
N_track = 6470
Elapsed time (s)
d.
Γ (µm²/s^α)
α
Hz_water 1.1 0.97
Hz_FV 0.17 0.64
Hz_40% glyc 0.27 1.0
Hz_60% glyc 0.10 1.0
TAMSD (µm²)
Elapsed time (s)
e.
Hz_40% glyc
Hz_60% glyc
Hz_FV
Bimodal fit
Unimodal fit
Probability Density (s^1/2/µm)
Normalized step size (µm/s^1/2)

Extended Data Figure 3: Single-particle tracking analysis of hemozoin motion. a, Image analysis comparing different conditions using same TAMSI methods as Fig. 1b. **b**, Viscosities and SPT parameters from glycerol:water ratios were confirmed by Stokes-Einstein equation with 0.4 µm radius nanobeads (NB) including a static localization error in single-particle tracking (σ). Blue lines indicate individual track time-averaged mean squared displacements (TAMSDs) with dashed black line showing weighted average. **c**, Blue lines indicate individual track TAMSDs with dashed black line showing weighted average. **d**, TAMSD. Error bars represent the standard deviation of the means of individual trajectories and are shown in grey. **e**, Probability density distribution of isolated crystals in 40% glycerol. Experimental step sizes showing difference between unimodal and bimodal fits.

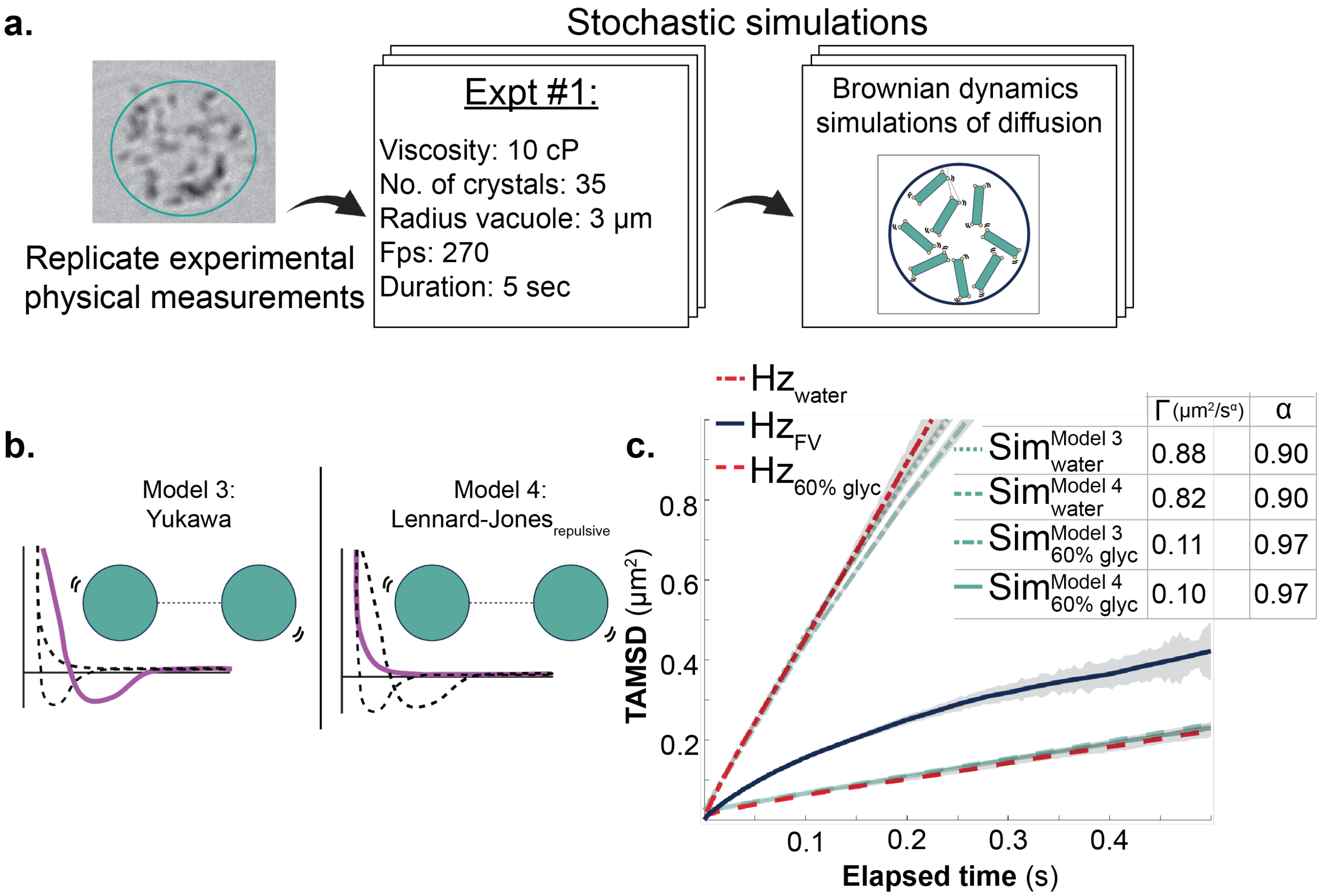

Extended Data Figure 4: Brownian dynamics simulations of hemozoin motion to test boundary effects and particle-particle interactions. **a**, Diagram showing example physical parameters that were used in each simulation, see Supplementary Table 6. The FV radius, expected viscosity, number of crystals, and frame rate of each experimental expanded FV was modeled. **b**, Additional particle-particle interactions were evaluated including the Yukawa potential and the repulsive term of Lennard-Jones applied to spheres. **c**, TAMSD of hemozoin crystals in expanded FVs compared to particles simulated with Brownian motion trajectories and interaction potentials using Models 3 and 4 from b. Error bars represent the standard deviation of the means of individual trajectories and are shown in grey.

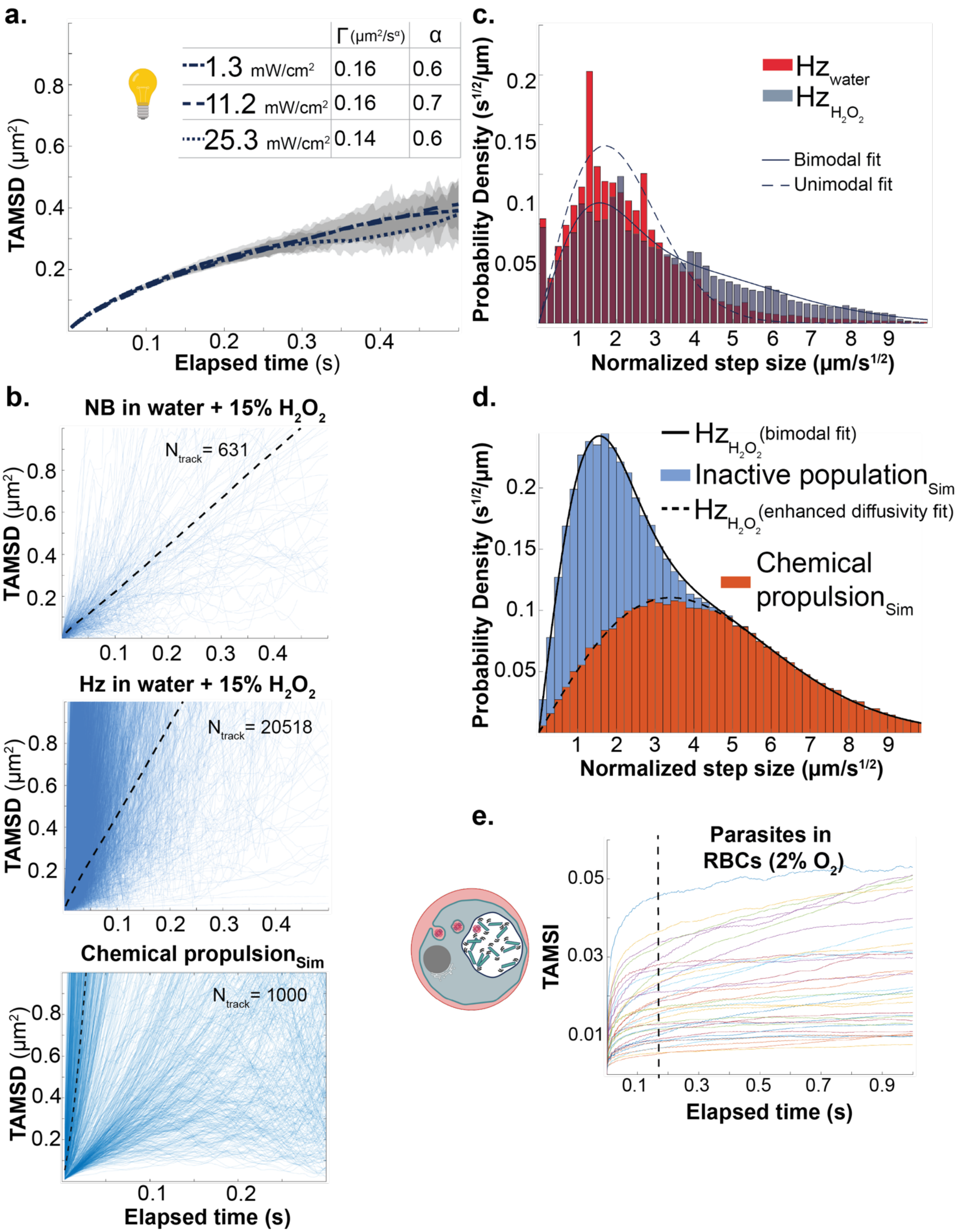
a.
Γ (μm²/sα)
α
1.3 mW/cm² 0.16 0.6
11.2 mW/cm² 0.16 0.7
25.3 mW/cm² 0.14 0.6
TAMSD (μm²)
Elapsed time (s)
b.
NB in water + 15% H2O2
Ntrack = 631
Hz in water + 15% H2O2
Ntrack = 20518
Chemical propulsionSim
Ntrack = 1000
TAMSD (μm²)
Elapsed time (s)
c.
Hzwater
HzH2O2
Bimodal fit
Unimodal fit
Probability Density (s1/2/μm)
Normalized step size (μm/s1/2)
d.
HzH2O2(bimodal fit)
Inactive populationSim
HzH2O2(enhanced diffusivity fit)
Chemical propulsionSim
Probability Density (s1/2/μm)
Normalized step size (μm/s1/2)
e.
Parasites in RBCs (2% O2)
TAMSI
Elapsed time (s)

Extended Data Figure 5: Impact of light and hydrogen peroxide on hemozoin motion. a, TAMSD of hemozoin crystals in expanded FVs under different measured light intensities. Error bars represent the standard deviation of the means of individual trajectories and are shown in grey. **b**, Blue lines indicate individual track TAMSDs with dashed black line showing weighted average. Lowest TAMSD shows simulated tracks from chemical propulsion model. **c,** Experimental step sizes showing difference between unimodal and bimodal fits. **d,** Histogram of step-size distribution simulated using a propulsion model. Step sizes of active population (orange) closely fit the expected step sizes for a particle with a diffusion coefficient of 5.8 $\mu m^2/s$ (dashed line). Adding the step sizes of the purely diffusive population (blue) the total distribution closely matches the bimodal fit for hemozoin in 15% peroxide from Table 5 (solid line). **e**, Cumulative data from different time lapse experiments indicating a constant elapsed time (~0.18 s) was chosen to determine velocities of all conditions.

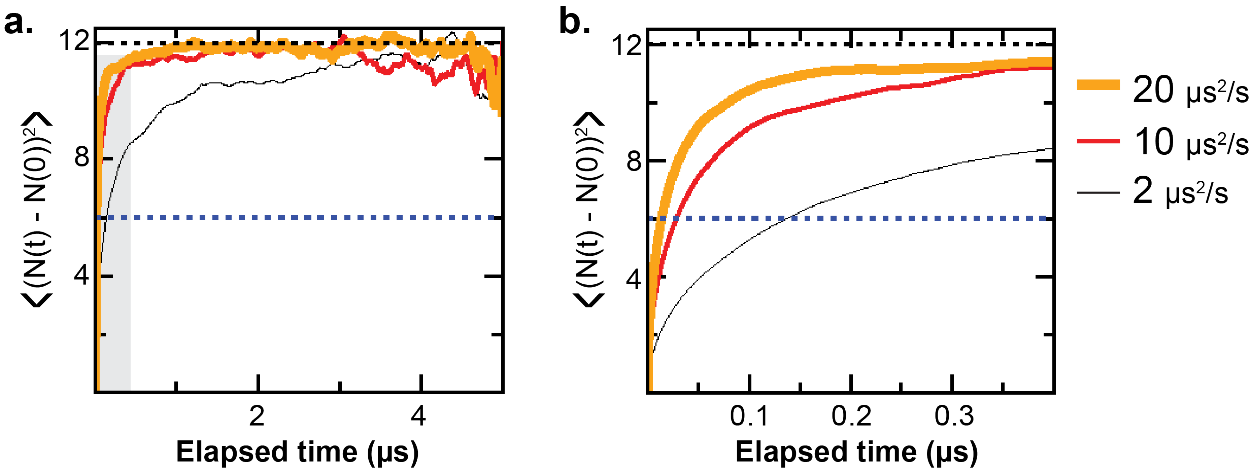

Extended Data Figure 6: Relaxation time of time-averaged mean squared pixel intensity change serves as proxy of diffusion coefficient. a, Dependence of time-averaged mean squared pixel intensity change (TAMSI) changes with diffusion coefficient obtained from Brownian dynamics simulations. **b**, Zoom into the region in which the curves cross the vertical line denoting half of the plateau value (blue).